

AN INVESTIGATION OF FLOW RATE MOTIVATED MOBILIZATION OF ENTRAPPED
ORGANIC LIQUIDS IN TWO-FLUID PHASE POROUS MEDIUM SYSTEMS

Ranxin Tao

A thesis submitted to the faculty at the University of North Carolina at Chapel Hill in partial fulfillment of the requirements for the degree of Master of Science in the Department of Environmental Sciences and Engineering.

Chapel Hill
2016

Approved by:
Cass T. Miller
Marc Serre
William Vizuite

© 2016
Ranxin Tao
ALL RIGHTS RESERVED

ABSTRACT

Ranxin Tao: An Investigation Of Flow Rate Motivated Mobilization Of Entrapped Organic Liquids In Two-Fluid Phase Porous Medium Systems
(Under the direction of Cass T. Miller)

Groundwater is one of the nation's most important natural resources, composing a large portion of total freshwater on earth. Therefore, groundwater contamination is a growing concern among groundwater hydrologists and the general public. Organic contaminants, often present as non-aqueous phase liquid (NAPL) in the groundwater, are major groundwater contaminants of concern. The purpose of this work was to investigate the mobilization of entrapped disconnected NAPL in porous medium systems. Tetrachloroethylene (PCE) was chosen as a model NAPL compound. Fluid properties of PCE were analyzed and column experiments as well as lattice Boltzmann simulations were performed to determine the relationships between residual NAPL saturation, fluid properties, and viscous forces. Trapping number (N_T) was tested as a criterion to predict and validate residual NAPL mobilization in porous media. Residual saturation was found to decrease with increasing viscous forces and N_T . The experimental data and simulation results were compared and showed good agreement.

TABLE OF CONTENTS

LIST OF TABLES	vii
LIST OF FIGURES	viii
CHAPTER 1: INTRODUCTION	1
1.1. Groundwater System	1
1.2. Groundwater Contamination	2
1.2.1. NAPL	3
1.2.2. Types of Contamination	4
1.2.3. Sources of Contamination	5
1.2.4. Remediation Methods	6
1.3. Single-phase Flow	8
1.3.1. Darcy's Law	8
1.3.2. Darcy-Forchheimer Law	9
1.3.3. Reynolds Number	10
1.4. Multiphase Flow	11
1.4.1. Interfacial Tension and Contact Angle	11
1.4.2. Darcy's Law for Multiphase Flow	11
1.4.3. Capillary Pressure	12
1.4.4. Capillary Number, Bond Number and Trapping Number	13
1.5. Turbulence	15

1.6. Modeling Approaches	16
1.7. Research Objectives	17
CHAPTER 2: EXPERIMENTAL METHODS	18
2.1. Experimental Materials	18
2.2. Column Experiments	19
2.2.1. Generator Column	19
2.2.2. Experimental Column	20
2.2.3. Tracer Tests	22
2.2.4. PCE Saturation Experiments	22
2.3. Analytical Methods	24
2.3.1. Interfacial Tension	24
2.3.2. Contact Angle	25
2.3.3. PCE Analysis	25
2.3.3.1. PCE Extraction	25
2.3.3.2. HPLC Methods	26
2.3.3.3. Calibration Curves	26
2.3.4. Lattice Boltzmann Methods	26
CHAPTER 3: EXPERIMENTAL RESULTS	30
3.1. PCE Properties	30
3.1.1. PCE solubility in distilled water	30
3.1.2. Interfacial Tension and Contact Angle	30
3.2. Column Experiments	31
3.2.1. Parameters for Column Packings	31

3.2.2. Tracer Test Results	32
3.2.3. Uniform Sand Column Results	32
3.2.4. High-Variance Sand Column Results	34
3.3. Lattice Boltzmann Results	39
CHAPTER 4: DISCUSSIONS	45
4.1. NAPL Mobilization Mechanisms	45
4.2. Comparison of Simulation and Experimental Results	47
4.3. Significance of Findings	55
CHAPTER 5: CONCLUSIONS	57
BIBLIOGRAPHY	60

LIST OF TABLES

2.1	The determined values for σ and φ_s for each experimental porous medium system	27
3.1	Fluid properties of PCE	30
3.2	Parameters for all different column packings	31
3.3	Experimental data of the PCE saturation experiments of the uniform sand column	33
3.4	Experimental data of all PCE saturation experiments	36
3.5	Lattice Boltzmann simulation data	40
4.1	N_{Ca} , N_B and N_T for each PCE saturation experiment	49
4.2	Table 4.2: N_{Ca} , N_B and N_T for each PCE saturation simulation	51

LIST OF FIGURES

2.1	Generator column	19
2.2	Experimental column	21
2.3	Procedures of PCE saturation experiments	24
2.4	The synthetic representation of the experimental porous medium constructed from a packing of 2,500 spheres with a porosity of 0.34 and a log radii variance of 0.2	27
3.1	Tracer test results for HV3 and HV4	32
3.2	Plot of the experimental data for the uniform sand column	34
3.3	Plot of the experimental data of HV1, HV2 and HV3 using PCE #1	37
3.4	Plot of the experimental data of HV4 using PCE #2	38
3.5	Plot of the experimental data of HV4 using SA-saturated PCE #3	38
3.6	Plot of the experimental data of all columns using different PCE	39
3.7	Plot of experimental and simulation data of PCE #1	41
3.8	Plot of normalized experimental and simulation data of PCE #1	41
3.9	Plot of experimental and simulation data of PCE #2	42
3.10	Plot of normalized experimental and simulation data of PCE #2	42
3.11	Plot of experimental and simulation data of SA saturated PCE #3	43
3.12	Plot of normalized experimental and simulation data of SA saturated PCE #3	43
4.1	NAPL entrapped in porous media. At left, a 2D image of NAPL droplets in a porous medium system. At right, a 3D representation of a single NAPL droplet	45
4.2	Plot of saturation (non-normalized) vs N_T for experiments	49
4.3	Plot of saturation (normalized) vs N_T for experiments	50

4.4	Plot of saturation (non-normalized) vs N_T for simulation	52
4.5	Plot of saturation (normalized) vs N_T for simulation	52
4.6	Turbulence in the simulated system at an Re of 220	55

CHAPTER 1: INTRODUCTION

1.1 Groundwater System

Groundwater refers to water that is found beneath the Earth's surface, filling in the cracks and pores in soil, sand, and rocks. As a part of the water cycle, groundwater is recharged from natural sources, including deep percolation from precipitation, seepage from streams and lakes, and groundwater flows in the subsurface, and it may eventually discharge into surface waters such as streams and lakes [1, 2].

Subsurface water can be divided vertically into zones depending on the relative proportion of the pore space occupied by water: a zone of aeration, in which the pores contain both gases and water, and a zone of saturation, in which all pores are completely filled with water. The saturated zone is bounded above by a surface called water table, on which the pressure of the water is atmospheric. In groundwater hydrology, the term groundwater is often used to denote, in particular, water in the zone of saturation [3].

Groundwater makes up 1.7% of the total water on earth, while ground freshwater makes up 0.76% of total water, which is 30.1% of total freshwater [4]. Groundwater is often withdrawn for agricultural, municipal, and industrial use and provides the largest source of usable water storage in the United States [6]. According to U.S. Geological Survey (USGS), the United States consumes 79.6 billion gallons of fresh groundwater for agricultural, municipal, and industrial purposes per day [5]. Among these uses, irrigation accounts for the largest consumption of groundwater in the United States [26]. The National Ground Water Association (NGWA) has

determined that 44% of the U.S. population depends on groundwater for its drinking water supply [27].

In a groundwater systems, flow takes place through a porous medium, which is defined as a system that consists of a continuous solid skeleton and a connected pore space that allows one or more fluids to flow through it [9]. A porous medium is characterized by morphology which includes geometric properties such as particle or pore shape and volume, and topology such as pore interconnectivity [35]. Porous medium flow is classified as single-phase, or two-phase, or multiphase depending on the number of immiscible fluid phases involved [9]. Compared to rivers and lakes, transport in porous media is generally slow and spatially variable due to heterogeneities in the medium [8]. The movement of groundwater is influenced by porosity, permeability, gravity, and pressure gradients. Mathematically, the velocity of groundwater flow can be described by Darcy's law which will be introduced in Section 1.3.1. Processes that occur routinely in porous medium systems can be described mechanistically using the fundamental equations of mass, momentum, and energy conservation [9].

1.2 Groundwater Contamination

Groundwater contamination may be defined as the artificially induced degradation of natural groundwater quality [11]. A wide variety of contaminants from a large number of sources can cause degradation of groundwater quality, ranging from petroleum products to microbial pathogens. A complete list and illustration of groundwater contamination types and sources will be presented in Section 1.2.2 and Section 1.2.3 respectively.

Most groundwater contamination incidents involve substances released at or only slightly below the land surface. There are at least four ways by which groundwater contamination occurs: infiltration (water percolates downward through a contaminated zone forming the leachate and

continue to migrate downward into groundwater), direct migration (contaminants migrate directly into groundwater from below ground sources), interaquifer exchange (contaminated groundwater mixes with uncontaminated groundwater), and recharge from surface water [18]. Soil can filter particulate matter out of water during infiltration but dissolved chemicals can still make their way into groundwater. Through these four ways, contaminants can occur in large enough concentrations in groundwater to cause problems and can be very difficult and costly to remediate [15].

The main groundwater contaminants of concern include petroleum hydrocarbons such as benzene, toluene, and xylene; chlorinated organics such as tetrachloroethylene (PCE), trichloroethylene (TCE) and its associated daughter products; heavy metals such as lead, zinc, and chromium; and certain inorganic salts [16]. Some of these contaminants are soluble and will dissolve readily in water (i.e. hydrophilic), in contrast, other contaminants are less soluble in water (i.e. hydrophobic). Many contaminants we wish to remove from water are hydrophobic, particularly when the hydrophobic contaminant is present as a separate liquid phase, it is referred as a non-aqueous phase liquid (NAPL).

1.2.1 NAPL

NAPL is a liquid solution that does not mix easily with water. Many common groundwater contaminants, including chlorinated solvents and many petroleum products, enter the subsurface as NAPLs [28]. NAPLs form a visible, separate oily phase in the subsurface whose migration is governed by viscous, gravity/buoyancy, and capillary forces. Because of the variety in their chemical composition, NAPLs behave very differently and can be generally classified as either a DNAPL or an LNAPL. DNAPLs, such as PCE, TCE, and manufactured gas plant (MGP) tars, are denser than water, and will tend to sink once they reach the water table. In contrast, LNAPLs,

such as gasoline and some industrial solvents, are less dense than water, and will tend to float on the water table [16, 29, 30].

NAPL droplets are trapped in porous media when capillary forces are greater than the mobilizing forces acting on the drop [33, 34]. Capillary forces make it extremely difficult or impossible to remove all the NAPL that have been released to the subsurface. For example, in petroleum recovery operations, pumping alone typically removes less than one-third of the oil in a petroleum reservoir, and even enhanced techniques such as water flooding or the application of surfactants can bring only 50% to 80% of the NAPL to the surface under optimum conditions. These recovery rates are acceptable to the oil industry. However, removal of much more than 99% of NAPL is probably required in order to restore a contaminated aquifer to drinking water standards, which is impractical without developing remediation technologies [17]. Rao et al. (1997) conducted a field-scale *in situ* cosolvent flushing at Hill Air Force Base in Utah to remove more than 85% NAPL [14]. Mulligan et al. (2001) wrote a review on surfactant-enhanced NAPL remediation, which included 22 field experiments, only one of them reported a recovery rate of 99%, most of them reported a recovery rate between 80% and 90% [13].

1.2.2 Types of Contamination

Based on different chemical compositions, groundwater contamination can be classified into six major types: (1) radionuclides, (2) tracer elements, (3) nutrients, (4) other inorganic species, (5) organic contaminants, and (6) microbial contaminants.

Radioactive contaminants, such as uranium (^{235}U), come from the nuclear industry throughout the nuclear fuel cycle, including mining and milling of uranium, uranium enrichment and fuel fabrication. Radioactive materials are carcinogenic to those who are subjected to long-term or large dose exposure and can cause genetic defects to their offspring. Trace metals, especially

heavy metals such as lead, cadmium, chromium and mercury, derive from mining effluents, industrial waste water, agricultural wastes and fossil fuels. These toxic substances can accumulate inside human bodies and may potentially be lethal. Nutrients are referred to as ions or organic compounds containing nitrogen or phosphorous. They result from agricultural practice including the use of fertilizers, cattle feeding and sewage, can cause methemoglobinemia and form carcinogenic compounds. Other inorganic species include metals present in non-trace quantities such as Ca, Mg, and Na plus nonmetals such as Cl and F, which originate from saline brine, mining, sanitary landfills and industrial waste water. These are generally not harmful, but exposure to high concentrations, especially Na, may disrupt cell and blood chemistry. Organic contaminants include chlorinated organics (such as PCE and TCE), petroleum hydrocarbons (such as benzene, toluene, and xylene), and pesticides which result from petroleum extraction, industrial and agricultural waste water. They can cause various kinds of health problems including cancer, liver damage, and brain disorders. Biological contaminants including pathogenic bacteria, viruses, or parasites, which come from human and animal sewage or waste water, can cause serious health conditions such as typhoid fever, cholera, polio and hepatitis [62].

1.2.3 Sources of Contamination

Sources of groundwater contamination are widespread. Examples include thousands of accidental spills, landfills, surface waste ponds, above or under-ground storage tanks, pipelines, injection wells, land application of waste and pesticides, septic tanks, radioactive waste disposal sites, salt water intrusion, and acid mine drainage, etc [16].

Based on a 1984 report by the Office of Technology Assessment (OTA) [71], the major sources of groundwater contamination can be divided into seven major categories, which are: (1) sources designed to discharge substances, e.g., septic tanks and injection wells; (2) sources

designed to store, treat, and/or dispose of substances; (3) discharge through unplanned release, e.g., landfills, surface impoundment, above or under-ground storage tanks and radioactive waste disposal sites; (4) sources designed to retain substances during transport or transmission, e.g., pipelines; (5) sources discharged as consequence of other planned activities, e.g., pesticide/fertilizer applications and mine drainage; (6) sources providing conduit or inducing discharge through altered flow patterns, e.g., production wells; and (7) naturally occurring sources whose discharge is created and/or exacerbated by human activity, e.g., salt water intrusion [16, 62].

In practice, the terms point and nonpoint are used to describe the degree of localization of the source. A point source is characterized by the presence of an identifiable, small-scale source, such as a leaking storage/septic tank, a disposal pond, a sanitary landfill or an accidental spill. In contrast, a nonpoint source is characterized by large-scale, relatively diffuse contamination originating from many smaller sources. Infiltration from farm land treated with pesticides and fertilizers is an example of a non-point source [62].

1.2.4 Remediation Methods

Many remediation methods, including physical and chemical remediation methods and bioremediation methods, are available to treat groundwater contamination. The most common remediation technologies are pump and treat, *in situ* air sparging, *in situ* flushing, permeable reactive barriers, and bio-based technologies.

Pump and treat has been the most conventional method for groundwater remediation since it came into wide use in the early to mid-1980s. The contaminated groundwater is pumped directly out of the surface and treated above ground, then the cleaned water is either discharged into a sewer system or re-injected into the subsurface [19]. Pump-and-treat systems have been operated

at numerous sites for many years, through which their performances have been evaluated and the results have shown that it is not very effective at cleaning up contaminated sites because it takes a very long time (years to decades, depending upon local factors, contaminants, and cleanup standards) and can require a large volume of water to remove a majority of contaminants [63, 64, 65, 66]. In addition, it is especially inefficient for certain situations, such as those with significant accumulations of DNAPLs trapped below the water table in heterogeneous media [63]. Due to its limitations, the pump-and-treat method is now primarily used for free product recovery and control of contaminant plume migration [19].

In situ flushing is the injection or infiltration of an aqueous solution (can be plain water, surfactant or cosolvent) into a zone of contaminated soil/groundwater via injection wells, followed by downgradient extraction of groundwater and above-ground treatment before discharge or re-injection [19, 67]. *In situ* flushing is designed to enhance conventional pump-and-treat by greatly reducing the time and amount of water used by mobilizing the sorbed contaminants. It is applicable to a wide variety of contaminants, and is not limited to the contaminant depth or location within the hydrogeological regime [67]. The effectiveness of this method depends strongly on the ability of the solution to desorb, solubilize, and/or flush the contaminants.

Other remediation methods like *in situ* air sparging and permeable reactive barriers are not within the scope of related knowledge of this research. During the implementation of air sparging, a gas is injected into saturated soil zone below the lowest known level of contamination. The gas contacts with the contamination, stripping the contaminant away or assisting in *in situ* degradation. A permeable reactive barrier is a wall containing an appropriate

reactive material placed across the path of a contaminant plume. It either removes or degrades contaminants as contaminated water passes through it [19].

Choosing a remedial technology is a function of the type of contaminant, site hydrogeology, source characteristics, and the location of the contaminant in the subsurface. Among those factors, the variation of hydraulic conductivity or transmissivity of a formation is one of the most important parameters of interest [16].

1.3 Single-phase Flow

1.3.1 Darcy's Law

Single-fluid-phase flow through a porous medium system is typically defined using Darcy's law. Darcy's law, first determined experimentally and reported by Henry Darcy in 1856 [10], is an equation that relates fluid pressure to flow rate in porous medium systems. It states that the volumetric flow rate through a column of porous material (Q) is proportional to the head loss across the sand column (h_2-h_1) and the cross-sectional flow area (A) and inversely proportional to the packed height of the column (L) [42], which can be written as

$$Q = KA \frac{h_2 - h_1}{L}$$

of which the differential form is expressed as

$$Q = -KA \frac{dh}{dL}$$

where a minus sign has been introduced because flow is in the direction of decreasing head. In these two algebraic expressions, K is referred to as the hydraulic conductivity, which serves as a measure of the permeability of the porous medium with [11, 42]

$$K = \frac{k\rho g}{\mu}$$

where k is the intrinsic permeability, which is determined for each porous medium system and depends on the distribution of the sizes, shapes, and orientations of the pores that provide pathways for flow within the solid system (i.e., the morphology and topology of the pore space) [42], ρ is the fluid density, g is the magnitude of the gravity vector and μ is the dynamic viscosity of the fluid.

The specific discharge, or Darcy velocity, can be written as:

$$q = \frac{Q}{A}$$

The average macroscale pore velocity is related to the specific discharge by

$$v = \frac{q}{\alpha}$$

where α is the effective porosity.

Additionally, for single-phase, three-dimensional flow through an isotropic medium where a body force per unit volume is present, the Darcy's law is typically expressed as

$$\mathbf{q} = -\frac{k}{\mu}(\nabla p - \rho \mathbf{g})$$

where \mathbf{q} is the volumetric flow rate per unit area vector and \mathbf{g} is the gravity vector.

1.3.2 Darcy-Forchheimer Law

Darcy's law correctly describes the fluid flow through porous media in the low velocity regime, however, as the flow velocity increases, a discrepancy between experimental data and the results obtained from Darcy's law begins to appear. After investigation, Philip Forchheimer (1901) linked this discrepancy to inertial effects [41]. In order to account for these high velocity inertial effects, he suggested adding an inertia term representing the kinetic energy of the fluid to the Darcy equation, and corrected the Darcy equation into the Forchheimer equation [43, 44, 45], which can be expressed as

$$\frac{dp}{dx} = -\frac{\mu}{k}q - \beta\rho q^2$$

where β is called the Forchheimer coefficient.

1.3.3 Reynolds Number

In a high velocity regime where the inertial effects become important, the flow begins to transition from Darcy flow to Forchheimer flow. Hence, criteria to identify the beginning of non-Darcy flow and the range of validity of Darcy's law are needed. One of these criteria is the Reynolds number (Re). Re, which is named after Osborne Reynolds, serves as a criterion to help predict similar flow patterns in different fluid flow situations [39, 73]. It is physically the dimensionless ratio of the inertial force to the viscous force [11], which is given by

$$\text{Re} = \frac{\rho v L}{\mu}$$

where ρ is the density of the fluid, v is the (average) fluid velocity, L is a characteristic linear dimension, which is the mean grain size in porous media, and μ is the dynamic viscosity of the fluid.

According to Todd (2005), experiments show that Darcy's law is valid for $\text{Re} < 1$ and is generally accurate up to $\text{Re} = 10$ [47], thus he determined $\text{Re} = 10$ as the upper limit to the validity of Darcy's law [11]. However, it is not an exact value. Zeng (2006) concluded that the critical Re may range from 1 to 100 based upon a comprehensive review of the literature [44].

For Darcy-Forchheimer law, Irmay (1958) reported that at low Re ($\text{Re} < 1$), the inertia term of the Forchheimer equation may be neglected, at medium Re ($1 < \text{Re} < 100$), the inertia term is of same order as the first term, at larger Re ($\text{Re} > 100$), the inertia term gradually becomes dominant and at very large Re, the first term may be neglected [43].

1.4 Multiphase Flow

1.4.1 Interfacial Tension and Contact Angle

Interfacial tension (IFT) and contact angle are two important properties to describe a multiphase system. IFT is defined as the free surface energy at the interface formed between two immiscible fluids [68]. It is caused by the unbalanced forces of liquid molecules at the surface and the tendency of the liquid to maintain the lowest surface free energy. IFT is responsible for the shape of liquid droplets, which tends to be a sphere. Thus, IFT can be measured by analyzing the shape of the drop. Several methods currently used to measure IFT are based on this principle. The most commonly used one is the pendant drop method where the actual shape of a hanging drop is matched to theoretical simulations to compute the IFT [69, 70]. Liquid IFT is directly related to the capillary pressure (introduced in Section 1.4.3) across an NAPL-water interface and is a factor controlling wettability [49].

The contact angle is defined as the angle between the solid surface and the fluid-fluid interface and is usually measured in wettability studies [32]. There are multiple conventions with regard to measuring contact angles. A usual convention is to measure the angle through the bulk phase (as opposed to measuring through the drop). In this convention, large contact angles ($\gg 90^\circ$) correspond to high wettability with regard to the bulk fluid, and the drop will spread over a large area on the surface; while small ones ($\ll 90^\circ$) correspond to low wettability and the drop tends to minimize its contact with the surface and form a compact liquid droplet. Contact angle is, like IFT, related to the capillary pressure as well, and is actually defined in terms of IFT according to Young's Formula [68].

1.4.2 Darcy's Law for Multiphase Flow

Darcy's law for single phase flow has been given in Section 1.3.1, which is

$$\mathbf{q} = -\frac{k}{\mu}(\nabla p - \rho \mathbf{g})$$

For each phase in a multiphase flow, this equation can be directly extended to multiphase flow [48]. For phase α ,

$$\mathbf{q}_\alpha = -\frac{k_\alpha}{\mu_\alpha}(\nabla p_\alpha - \rho_\alpha \mathbf{g})$$

where α indicates that the physical quantity is for phase α .

The effective permeability for each phase is not greater than the intrinsic permeability k of the porous medium with [48]

$$k_\alpha = k_{r\alpha} k$$

where $k_{r\alpha}$ is the relative permeability which indicates the tendency of phase α to wet the porous medium.

Therefore, for phase α , Darcy's equation can also be written in terms of $k_{r\alpha}$ and k as

$$\mathbf{q}_\alpha = -\frac{k_{r\alpha} k}{\mu_\alpha}(\nabla p_\alpha - \rho_\alpha \mathbf{g})$$

1.4.3 Capillary Pressure

When two immiscible fluids are in contact in the pores of a porous medium, a pressure difference exists across the interface separating them. This pressure difference is called capillary pressure and is related to the IFT and curvature of the interface [3, 50]. The capillary pressure causes porous media to draw in the wetting fluid and repel the non-wetting fluid [49].

At the macroscale, capillary pressure is the product of average IFT and the average interfacial curvature [51]:

$$p^c = -\gamma^{wn} J_w^{wn}$$

where p^c is the average capillary pressure over the wn interface, γ^{wn} is the average IFT over the wn interface, and J_w^{wn} is the macroscale surface curvature defined as the average over the wn interface of the surface divergence of the outward normal from phase w .

Particularly, at equilibrium, the capillary pressure is given as [51]:

$$p^c = p^n - p^w$$

where p^n is the non-wetting phase pressure, and p^w is the wetting phase pressure. This equation is not valid for a dynamic system.

Capillary pressure has been found to closely relate to saturation and permeability. Pressure-saturation-permeability (p - S - k) relations are of central importance of modeling multiphase systems. Modeling of p - S - k relations can be subdivided into: (1) pressure-saturation (p - S) models, (2) saturation-permeability (S - k) models, and (3) hysteresis models. Attempts have already been made to derive these models. Several empirical and semi-empirical expressions of these models are available in the literature [52]. For example, laboratory experiments have shown that capillary pressure can be represented as a function of saturation [53]. The Brooks-Corey (1964) and van Genuchten (1980) models are two well-known empirical models that relate the capillary pressure to the saturation of the phases [50, 54].

1.4.4 Capillary Number, Bond Number and Trapping Number

There are three important dimensionless numbers in entrapped NAPL mobilization: the capillary number (N_{Ca}), the bond number (N_B) and the trapping number (N_T). The capillary number represents the ratio of viscous forces to capillary forces, the bond number represents the ratio of the gravity/buoyancy to capillary forces, and they are combined to form N_T with [33]:

$$N_T = \sqrt{N_{Ca}^2 + 2N_{Ca}N_B \sin \alpha + N_B^2}$$

where α is the angle the flow makes with the positive x axis.

For vertical flow ($\alpha = 90^\circ$), in the direction of the buoyancy force, their expressions can be expressed as [33]:

$$N_{Ca} = \frac{q_w \mu_w}{\sigma_{ow} \cos \theta},$$

$$N_B = \frac{\Delta \rho g k k_{rw}}{\sigma_{ow} \cos \theta}, \text{ and}$$

$$N_T = \sqrt{N_{Ca}^2 + 2N_{Ca}N_B + N_B^2} = |N_{Ca} + N_B| = \left| \frac{q_w \mu_w + \Delta \rho g k k_{rw}}{\sigma_{ow} \cos \theta} \right|$$

respectively, where q_w is the Darcy velocity of the aqueous phase, μ_w is the dynamic viscosity of the aqueous phase, σ_{ow} is the IFT between the organic liquid and water, θ is the contact angle, $\Delta \rho$ is the difference of the density between the aqueous phase and the organic phase, g is the gravity acceleration constant, k is the intrinsic permeability of the porous medium, k_{rw} is the relative permeability to the aqueous phase.

N_T quantifies the balance of gravitational, viscous, and capillary forces acting on an entrapped NAPL droplet, and was originally developed (discussed in more detail in Section 4.1) as a criterion to predict the onset and extent of residual NAPL mobilization in porous media. Many studies have since used N_T to predict or validate the occurrence of mobilization of trapped residual NAPL saturations in laboratory columns [33, 36, 91, 92, 93, 94, 95, 96, 77, 60, 56, 55, 46, 38]. Based on these studies, it has been well established that the residual saturation is a decreasing function of the N_T in NAPL mobilization. Thus, the goal for a mobilization based remediation technique is to increase N_T , which is typically accomplished by reducing σ_{ow} by adding cosolvents or surfactants to the aqueous flushing solution, or by increasing the flow rate [34].

1.5 Turbulence

In fluid dynamics, turbulence refers to a high velocity flow regime characterized by chaotic, stochastic property changes. The flow field of turbulence consists of a mean (time-averaged) component plus a random, chaotic motion [40].

A highly viscous or slow-moving fluid tends to be smooth and regular, which is called laminar flow. As the viscosity reduces, or the fluid velocity increases, the movement of the fluid becomes irregular and chaotic, which is called turbulent flow. This process is called the transition to turbulence and has been illustrated in a number of experiments such as Reynolds' experiments [39, 40, 73]. Laminar flow admits a steady flow field and tends to flow without lateral velocity, which means there are no cross currents perpendicular to the direction of flow. Due to the presence of lateral velocity, turbulent flow transports and mixes fluid much more effectively than a comparable laminar flow [39, 72]. During transition, the Re serves as a criterion to distinguish between laminar and turbulent flow. Laminar flow occurs at low Re where viscous forces are dominant, while turbulent flow occurs at high Re where inertial forces are dominant.

A steady state cannot be achieved when a flow is transitioning to the turbulent flow, due to the eddies that form in the system, the pressure field and the velocity field are constantly oscillating. These fields are three-dimensional, time-dependent and random, which makes it difficult to develop an accurate tractable theory or model. For a turbulence problem, there are no prospects of a simple analytic theory. Instead, hopes are placed on the use of ever-increasing power of digital computers [72].

Due to the fact that most groundwater flows are laminar, and researchers has focused on other aspects of the system that affect mobilization, such as IFT, the effect of turbulence on NAPL mobilization is seldom examined.

1.6 Modeling Approaches

A wide range of spatial scales are used when describing porous medium systems. These scales, from the smallest to the largest, are referred to, respectively, as the molecular scale, the microscale, the resolution scale, the macroscale, and the megascale [9]. Models may be developed at different length scales and are associated with the scale being considered. Most common models are formulated at the microscale and macroscale.

The microscale, also referred to as the pore scale, is the scale at which all details of the morphology and topology of the pore space and solid phase distribution are known, which means the location of each solid grain and the distribution of the fluid phases are resolved in space and time. At this scale, the length scale of the fluid system is much larger than that of a single molecule or its mean free path, and hence the fluid is considered as a continuum [7, 61].

The macroscale is the scale at which the details of the microscale are not available and a point represents the averaged condition in a region around the point. At the macroscale, we work with averaged quantities, such as porosity, which describes the pore space available at the microscale; as well as fluid saturation and permeability to describe systems. By averaging, the intricate variations due to the microscopic heterogeneity are smoothed out, and the system can be considered as an equivalent homogeneous system.

High-resolution imaging methods or computational approaches are used to create a model porous medium system at the microscale. Common techniques include: (1) pore network models, where the medium is viewed as a series of tubes, spheres, triangles, etc; (2) images of actual porous media, as captured by x-ray, MRI, etc; and (3) sphere packing algorithms, which create systems of spheres that match porosities and grain size distributions of the system of interest.

At the microscale, the Navier-Stokes equation can be approximated using numerical methods. Instead of solving the Navier-Stokes equation, the lattice Boltzmann method (LBM) can be used to solve the discrete Boltzmann equation to simulate the flow of a Newtonian fluid with collision models [58, 37]. According to several reviews by Benzi et al. (1992), Chen et al. (1998) and Aidun et al. (2010), LBM has been applied to various flow conditions including two-dimensional, three-dimensional turbulence, and multiphase flows through porous media [57, 58, 59].

Microscale modeling offers an important tool to understand pore-scale flow and transport processes that influence the macroscopic behavior. However, the modeling approaches are computationally intensive and are not feasible to be used to simulate a system where the characteristic length is on the order of meters or longer. Therefore, upscaling approaches such as thermodynamically constrained averaging theory (TCAT) are implemented to manifest the microscopic processes at larger spatial scales [9, 12].

1.7 Research Objectives

The overall goal of this work is to investigate the mobilization of an entrapped disconnected non-wetting phase (NWP) in porous medium systems. The specific objectives are: (1) to investigate experimentally the effect of viscous forces in mobilizing entrapped NWP; (2) to evaluate the effect of IFT and contact angle on mobilization of entrapped NWP; (3) to determine the influence of turbulence on NWP mobilization; (4) to model NWP mobilization; and (5) to compare experimental observations and pore-scale modeling of NWP mobilization.

CHAPTER 2: EXPERIMENTAL METHODS

2.1 Experimental Materials

All reagents used, including isopropanol (IPA), tetrachloroethylene (PCE), acetonitrile, and dibenzothiophene (DBT), were ACS reagent grade or better. A 12/20 mesh Accusand ($d_{50} = 1.105 \pm 0.014$ mm, uniformity coefficient = 1.231 ± 0.043 , $\rho = 2.655$ g/cm³, hydraulic conductivity = 0.503 ± 0.017 cm/s) and a polydisperse sand mixture composed of 11 different grain sizes ranging from 0.35 mm to 3 mm and following a log-normal particle size distribution with a mean diameter of 1.15 mm and a variance of 0.52 mm, were used in the column experiments.

Three batches of PCE produced by Fisher, Sigma-Aldrich and J.T. Baker were used in the experiment and are marked as PCE #1, PCE #2 and PCE #3 respectively. The fluid properties of these three batches of PCE will be discussed in detail in Section 3.1. Additionally, stearic acid (SA) was used to reduce the IFT and increase the contact angle of PCE. SA has a low water solubility (0.6 mg/L; Yalkowsky and He 2003) [20], minimizing loss from the PCE during water flushing. PCE was colored with an organic soluble dye, Oil-red-o, at a concentration of 0.01% for visualization purposes. Previous studies have shown that the addition of Oil-red-o dye to PCE did not significantly alter the IFT [77], and the slight change in measured IFT did not alter the potential for PCE displacement during flushing [33]. All the experiments were conducted at a temperature of $22 \pm 1^\circ\text{C}$.

2.2 Column Experiments

2.2.1 Generator Column

A generator column composed of a large metal column with 10.2-cm inner diameter and 110 cm total length was used to generate PCE-saturated water for the experimental column. The column was filled with 75 cm of 12/20 Accusand, which had a porosity of 0.43. The total pore volume of the column was calculated by adding the volume of the unfilled part and the pore volume of filled part, which was found to be 5.5 L. The inlet of the generator column was connected to a nitrogen-pressurized water tank with polytetrafluoroethylene (PTFE) tubing. A rotameter was installed between the water tank and the generator column to allow control of the flow rate. The water in the tank was driven by the pressure created by a compressed nitrogen tank, and entered the generator column through the PTFE tubing. As the water flowed upward through the generator column, the solution became saturated with the PCE that was entrapped in the porous medium. The generator column setup is shown as Fig 2.1.

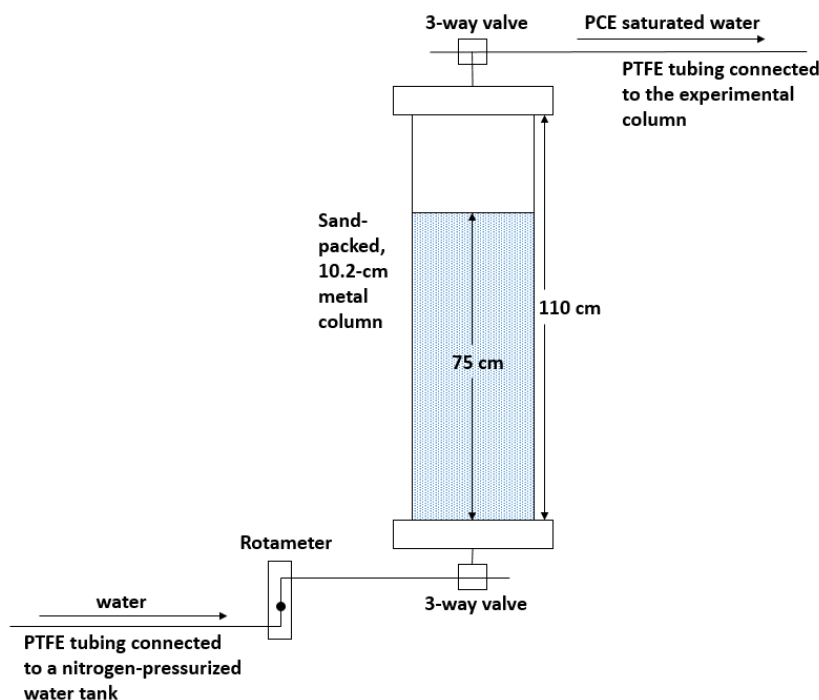


Fig 2.1: Generator column

After the column was packed with sand, dyed PCE was then injected into the column from the bottom, then water was flushed upward through the column at 1500 mL/min to make sure the PCE was dispersed evenly within the sand and any mobile PCE was removed. Once no visible PCE eluted from the column, the effluent was collected and the concentration of dissolved PCE was measured using high-performance liquid chromatography (HPLC). The results were averaged and compared with the result from a batch test to determine if the effluent from the generator column had been saturated with PCE. The batch test involved mixing PCE with distilled water at a 1:5 volume ratio in three centrifuge tubes, shaking for over 12 hours, and measuring the dissolved PCE concentration by HPLC to determine the solubility of PCE in distilled water.

2.2.2 Experimental Column

Column experiments were conducted in a vertically oriented glass column with 2.5-cm inner diameter (ACE Glass), as shown in Fig 2.2. The column was set up by first inserting a PTFE plunger with a wetted o-ring seal and a steel mesh filter into the bottom of the column. Next, the porous medium was poured into the column while being stirred in order to keep all the grains evenly distributed, and the mass of porous medium added was recorded. Then, a second plunger with an o-ring and a glass frit was inserted into the top of the column and pushed in until firmly touching the sand.

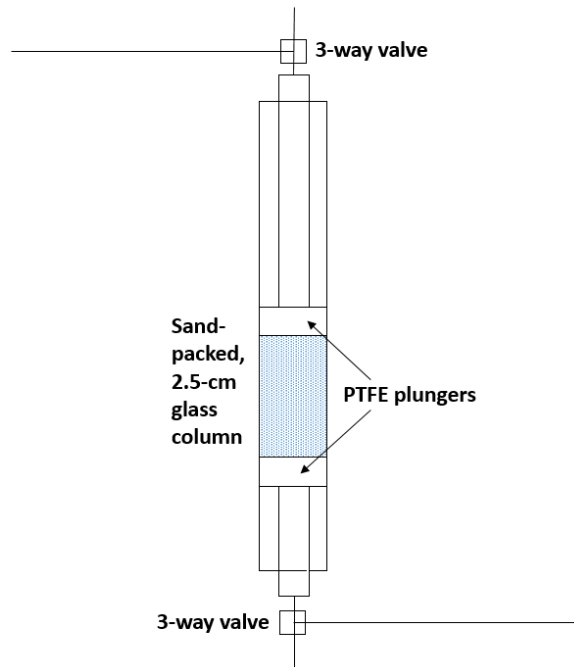


Fig 2.2: Experimental column

Each plunger contained a 0.45-cm inner diameter tubing that was connected to a three-way valve. Two programmable syringe pumps (Harvard Apparatus PHD 4400) were used to inject PCE, IPA and distilled water.

One uniform sand column packed with 12/20 Accusand and four high-variance sand columns (HV1, HV2, HV3 and HV4) packed with a polydisperse sand and a glass bead mixture with a log normal grain size distribution were packed during the course of the experiment work. For each of the columns, the length of the filled column was measured, and the mass of media added to the column was divided by the particle density of the porous medium to calculate the solid volume of the column. The pore volume was then determined by subtracting the solid volume from the total volume. Additionally, the porosity of the column was calculated by dividing the pore volume by the total volume of the column.

After the column was packed with porous media, CO₂ was then pumped through the column upwards to displace the air in the system. Next, distilled water was pumped through the column

upwards, at a rate of 20 mL/hr to displace the CO₂, until 10 pore volumes of water was moved through the system.

2.2.3 Tracer Tests

A series of tracer tests were performed on the experimental columns using a stock solution of tritiated water (T₂O), a radioactive form of H₂O where the hydrogen atoms are replaced with tritium (³H or T). The results of the tracer tests were used to identify if there was significant flow by-passing in a specific column packing during flushing.

Initially, T₂O was pumped upwards through the column at a flow rate of 10 mL/hr. Samples were collected in 20-mL plastic scintillation vials, which were numbered and weighed prior to the experiment. Samples were taken every 2.5 mL, or every 15 minutes, until more than 2.5 pore volumes of the experimental column had been pumped through the column in order to ensure that the distilled water in the experimental column was completely replaced with T₂O. The filled sample vials were then weighed again and mixed with 7.5 mL of scintillation cocktail (ScintiSafe 30% LSC-Cocktail) and analyzed on a scintillation counter (Packard 1900 TR Liquid Scintillation Analyzer) to determine the disintegrations per minute (DPM). Finally, this value for each sample was divided by the volume of the sample to find DPM per mL.

2.2.4 PCE Saturation Experiments

A series of specific flushing experiments were conducted on the experimental column to reveal the relationship between the flow rate of flushing and the entrapped saturation of PCE. Increasing the flow rate of water, increases the mobilizing viscous forces acting on the entrapped organic phase.

First, dyed PCE was pumped upward through a water-saturated column at a flow rate of 35 mL/min until the column was saturated with PCE. Then distilled water was pumped downward

at 20 mL/hr ($Re = 0.04$) to achieve the initial residual PCE saturation. Next, the column was flushed by PCE-saturated water upward for 85 – 100 PV to mobilize the PCE remaining in the experimental column. A series of flow rates was selected such that the corresponding Re ranged from 25 to approximately 225. The flow rate meter, which was connected to the generator column, was used to roughly estimate the current flow rate throughout the process in order to reach an expected flow rate. The flow rate was first adjusted by the rotameter, while PCE-saturated water was bypassing the experimental column through the 3-way valve on the bottom to get a steady flow rate. Then the valve was switched to allow flow into the column. The actual flow rate was determined by weighing the effluent and timing the experiment. Next, IPA was pumped downward to extract the PCE remaining in the column at a flow rate of 500 mL/hr. In order to avoid too much water being collected in the solution and thus affecting the HPLC analysis, a centrifuge tube was used to collect the effluent first and was then switched to a new centrifuge tube when the dissolved PCE approached the bottom of the column. The effluent was then analyzed for PCE by HPLC as described below in Section 2.3.3. At the completion of the experiment, 4L of PCE-saturated water from the generator column was pumped through the experimental column to restore the experimental column to its initial state. All the above steps are shown in Fig 2.3.

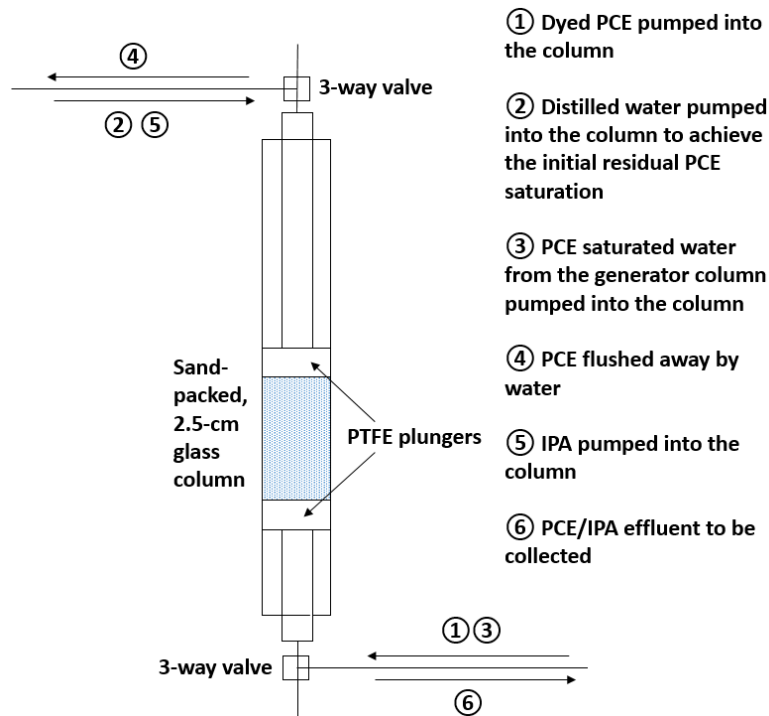


Fig 2.3: Procedures of PCE saturation experiments

For each column packing, a number of measurements of the PCE saturation after the 20mL/hr flow rate step were made to determine the initial residual PCE saturation and to make sure all the experiments had a similar initial state of PCE saturation.

2.3 Analytical Methods

2.3.1 Interfacial Tension

IFT was measured using the pendant drop method. A polycarbonate cuvette was filled with distilled water (pre-equilibrated with PCE), and a drop of PCE was suspended from a stainless steel needle. A digital video camera captured images of the drop, and Kruss's Drop Shape Analysis II (DSA2) software was used to determine the native IFT. IFT measurements were conducted using dyed (Oil-red-o) PCE.

IFT was measured with prior equilibration. Equilibration entailed combining the PCE and distilled water at a 1:5 volume ratio in a centrifuge tube, shaking for over 24 hours, then

centrifuging to separate the phases. Between each sample, the plastic cell was replaced with a new one.

2.3.2 Contact Angle

Contact angles were measured using the same instrumentation and software that were used for the IFT measurements. A drop was dispensed by needle on a 25×25 mm quartz slide (Chemglass) placed in the glass cell, then images were captured to measure the static (θ_s) contact angles (through the aqueous phase) on each side of the drop.

An inclined plate method was used to measure the advancing (θ_A) and receding (θ_R) contact angles, where exactly same steps were followed but the stage was tilted until the drop just began to move along the surface of the slide and images were captured immediately prior to the movement of the drop.

Contact angle measurements were conducted with the equilibrated PCE and aqueous phases. Between each sample, the glass cell and quartz slides were rinsed sequentially with acetone, methylene chloride, and acetone again, followed by a final, thorough distilled water rinse.

2.3.3 PCE Analysis

2.3.3.1 PCE Extraction

Effluent samples from the column experiments were collected in centrifuge tubes. The collected PCE/IPA solution was transferred to a 50-mL volumetric flask and diluted with IPA to 50 mL. A 0.5-mL aliquot was then transferred from the 50-mL volumetric flask to a 10-mL volumetric flask. An internal standard (1.2g DBT in 25ml acetonitrile) was added, and the solution was brought up to volume with IPA prior to analysis with HPLC.

2.3.3.2 HPLC Methods

Analysis was performed by HPLC (Water 600S controller, 616 pump, and 717 autosampler) equipped with a WatersTM 996 Photodiode Array Detector, a Thermo Scientific Hypersil Green PAH column (10 cm × 4.6 mm, 3 μ m packing), and HPLC grade solvents. The HPLC method used an isocratic flow program using 30% water, 70% acetonitrile at 1.00 mL/min. Both PCE and the internal standard, DBT, were measured at a wavelength of 223.0 nm.

2.3.3.3 Calibration Curves

PCE was quantified by HPLC using an internal standard method. Calibration was performed with six standard solutions containing PCE in concentration from 200 to 2000 mg/L, along with the internal standard. The PCE stock solution was made by dissolving 1 g PCE solution into a 100 mL IPA. The exact weight of PCE was measured and recorded. Then a series of PCE calibration solutions was made in a 10-mL volumetric flasks from the 100-mL stock solution. The data points were fitted to a linear equation that was used to calculate the concentration of PCE in experimental samples. All the calibration curves had an $R^2 > 0.99$ to ensure accuracy. PCE calibration curves for HPLC were made and updated every 2-3 weeks, in order to ensure the accuracy of the experiments.

2.3.4 Lattice Boltzmann Methods

Mobilization simulations matching the experimental conditions were carried out using a three-dimensional, 19-velocity-vector (D3Q19), multiple-relaxation time (MRT) lattice Boltzmann method [23]. A three-dimensional, synthetic representation of the porous medium used in the laboratory experiments was generated using a sphere packing algorithm [24]. The porosity and lognormal size distribution for the sphere radii of the sphere pack were set to match the experimental porous medium. The anisotropic sphere pack consisted of 2,500 spheres arranged

in a non-overlapping fashion with a porosity of 0.34 and a log radii variance of 0.2, as shown in Fig 2.4. The lattice size necessary to achieve a grid-independent solution was 520^3 , which corresponded to a 0.04-mm grid resolution.

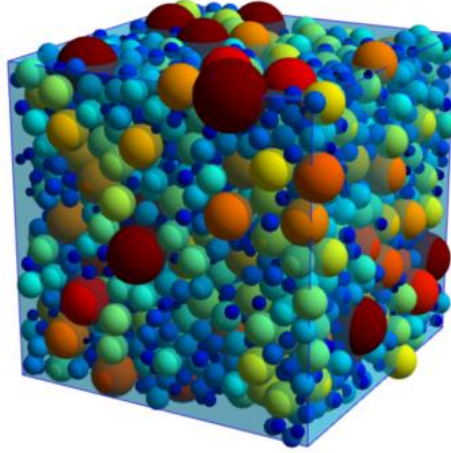


Fig 2.4: The synthetic representation of the experimental porous medium constructed from a packing of 2,500 spheres with a porosity of 0.34 and a log radii variance of 0.2.

In the LBM three parameters must be established: ζ , which controls the interfacial width, σ , which determines the IFT γ_{wn} , and φ_s , which controls the contact angle θ . A ζ of 0.9 was used based on previous analysis that concluded the parameter is independent of IFT. The parameters σ and φ_s were determined to match the experimental parameters using a bubble test in the absence of the solid phase and a constrained bubble test, respectively, as described in Dye et al. (2015) [25]. Table 2.1 lists the determined values for σ and φ_s for each experimental porous medium system.

PCE Batch	γ_{wn}	θ	σ	φ_s
1	37.03	32.76°	7.5×10^{-3}	0.29
2	35.68	43.78°	7.2×10^{-3}	0.41
3	25.77	66.19°	4.8×10^{-3}	0.54

Table 2.1: The determined values for σ and φ_s for each experimental porous medium system.

The initial conditions for the mobilization simulations were determined by simulating drainage and imbibition in the synthetic porous medium systems outlined in Table 2.1. A displacement simulation began with a fully wetting-phase-saturated system. Constant pressure boundary conditions were set on one face for one fluid and on the opposite face for the second fluid, with no-flow boundaries on all other boundaries. The simulation was performed by varying the pressure boundary conditions and allowing the system to reach an equilibrium state before the next step change in fluid pressures, where equilibrium was determined by the change in interfacial curvature. The microscale fluid density distribution was obtained for each equilibrium state and used to identify the regions of the pore-space occupied by the wetting (w) phase domain Ω_w , the non-wetting (n) phase domain Ω_n , and the wetting-non-wetting (wn) interfacial domain Ω_{wn} . All the phases and interfaces could be identified explicitly because the position of the solid (s) phase was known. After each entity was identified, the saturation of the non-wetting phase was computed according to

$$s^n \approx \frac{\sum_{X_k \in \Omega_n} 1}{\sum_{X_k \in \Omega_w \cup \Omega_n} 1}$$

where X_k denotes lattice site k . The state of the system at the end of imbibition was used as the initial condition for the mobilization simulations for a given synthetic porous medium system.

In the mobilization simulations, a constant velocity boundary condition was set on the inlet face and a periodic boundary condition on the outlet face of the system, with no-flow boundaries on all other boundaries. The velocity boundary condition on the inlet was set to match the experimentally measured flow rate of the wetting phase entering the column. Once the velocity boundary condition was established, the simulator was run until a set number of pore volumes of the wetting phase flowed out of the system. The number of pore volumes was set to match the

experimental conditions. The microscale fluid density was obtained for each mobilization simulation and used to compute the saturation of entrapped non-wetting phase that remained.

CHAPTER 3: EXPERIMENTAL RESULTS

3.1 PCE Properties

3.1.1 PCE solubility in distilled water

The solubility of PCE in distilled water was found to be 190 ± 20 mg/L in the batch test. Comparing this concentration with reported values in the literature tested the validity of the method. Gillham (1990) reported the solubility of PCE is 200 mg/L at 20°C [79]. Ladaa et al. (2000) measured the solubility of PCE in deionized water at 25°C, which was reported to be 215 ± 20 mg/L [21]. Mackay et al. (1993) quoted the measured solubilities of PCE in water to range from 150 up to 489 mg/L, which were determined using a variety of experimental methods [22]. These literature values are consistent with the measured value.

3.1.2 Interfacial Tension and Contact Angle

The fluid properties of the three different batches of PCE are summarized in Table 3.1.

Fluid	IFT (mN/m)	θ_S	θ_A	θ_R
PCE #1 (Fisher)	37.0 ± 0.8	$33 \pm 8^\circ$	$18 \pm 7^\circ$	$50 \pm 10^\circ$
PCE #2 (Sigma- Aldrich)	36 ± 2	$44 \pm 4^\circ$	$40 \pm 20^\circ$	$76 \pm 9^\circ$
SA-saturated PCE #3 (J.T. Baker)	26 ± 1	$70 \pm 10^\circ$	$50 \pm 20^\circ$	$94 \pm 4^\circ$

Table 3.1: Fluid properties of PCE

As shown in Table 3.1, the measured IFT values were similar for PCE #1 and PCE #2 (37 and 36 mN/m, respectively), and significantly lower for the SA-saturated PCE #3 (26 mN/m). As for the contact angles, an increasing trend in the measured values was found through PCE #1 to SA-saturated PCE #3. For the θ_S , PCE #1 and PCE #2 (33° and 44° , respectively) were relatively

close to each other, while SA-saturated PCE #3 had a much larger θ_s (70°) than PCE #1 and PCE #2.

Since the value of IFT depends strongly on the temperature, the measuring method and the instrumentation used, the literature values for the IFT between PCE and water vary, but the reported values are mostly higher than 43 mN/m [33, 77, 78, 82]. Despite careful and thorough cleaning of the instrumentation and repeated experimentations, the measured IFT remained lower than those literature values. However, Gioia (2006) reported an IFT of 36.5 mN/m for PCE [83], which is much closer to the measured IFT.

The reduction of the interfacial tension in SA-saturated PCE #3 is due to the affinity of the SA (a surfactant) for both hydrophilic and hydrophobic molecules [74]. The ability of SA to decrease IFT between the NAPL and aqueous phase has also been reported in other studies [75, 76].

3.2 Column Experiments

3.2.1 Parameters for Column Packings

Table 3.2 shows all the parameters for each column, including the column length, packing material, pore volume and porosity.

Column name	Column length (cm)	Packing material	Pore volume (mL)	Porosity
Uniform sand column	5.18	12/20 Accusand	8.52	0.335
HV1	7.78	A polydisperse sand and glass bead mixture	12.8	0.336
HV2	7.42		12.2	0.334
HV3	8.02		14.0	0.356
HV4	7.65		14.4	0.383

Table 3.2: Parameters for all different column packings

3.2.2 Tracer Test Results

The results of the tracer tests can be seen in Fig 3.1, which shows the results for gradually replacing distilled water with T₂O in HV3 and HV4, where the x-axis represents the ratio of the injected volume of T₂O to the pore volume of the system (the sum of the pore volume of the experimental column and the total volume of the tubing between the outlet and the pump) and the y-axis represents the ratio of the T₂O concentration to the injected concentration. The time for each test was started when the syringe pump was started.

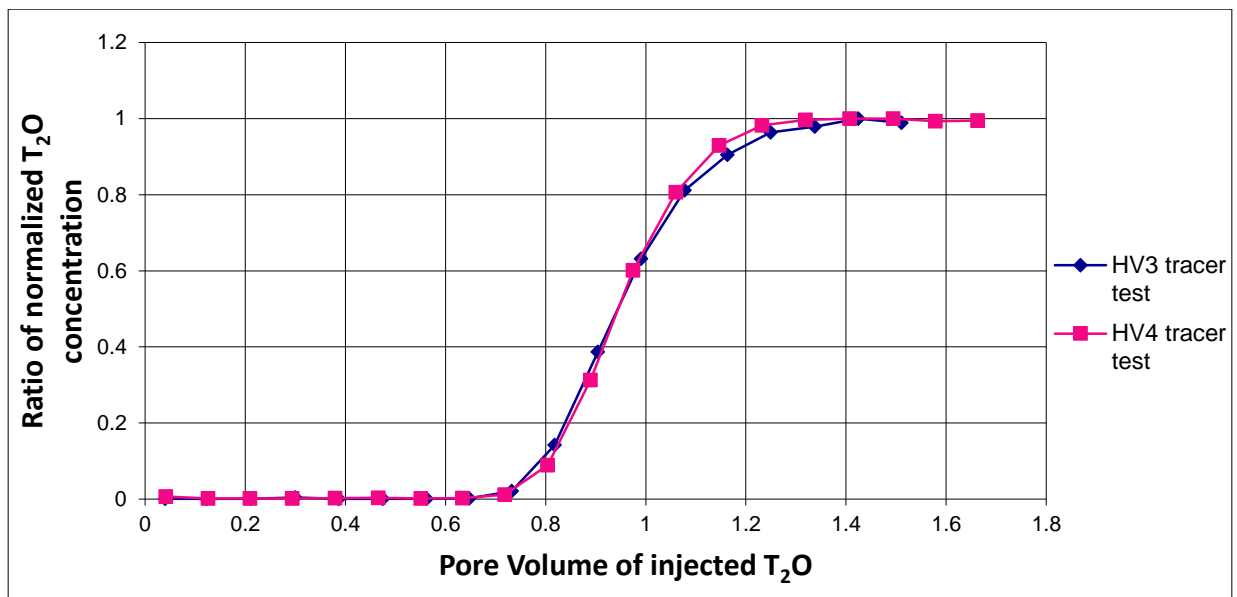


Fig 3.1: Tracer test results for HV3 and HV4

In Fig 3.1, both curves are reasonably symmetric and there is no evidence of significant flow by-passing in these two column packings.

3.2.3 Uniform Sand Column Results

A set of preliminary experiments was conducted with a column packed with 12/20 Accusand using PCE #1. At the beginning of the experiment, the PCE saturation in the experimental column approached 100%. Most of the PCE was removed during the 20 mL/hr water flush. After that stage, the rest of PCE were evenly dispersed as droplets in the experimental column. Then

during the high Re flushing, the PCE droplets were removed from the column rapidly after flushing began. Additional PCE-saturated water was pumped through the experimental column to ensure that steady-state had been reached. The residual remaining after flushing visually decreased as the Re number was increased. In very high Re flushing where $Re > 200$, nearly all visible PCE was mobilized from the experimental column. The experimental data of the PCE saturation experiments of the uniform sand column are shown in Table 3.3, and a plot of the results is shown in Fig. 3.2.

Re	PCE saturation
0.04	13.25%
0.04	12.78%
0.04	12.77%
0.04	12.51%
22.0	10.48%
142.3	7.75%
199.4	4.01%
216.2	2.26%

Table 3.3: Experimental data of the PCE saturation experiments of the uniform sand column

Based on the experimental data, the saturation after 20 mL/hr distilled water flushing was $12.8 \pm 0.5\%$, which served as the starting point for the subsequent high Re experiments.

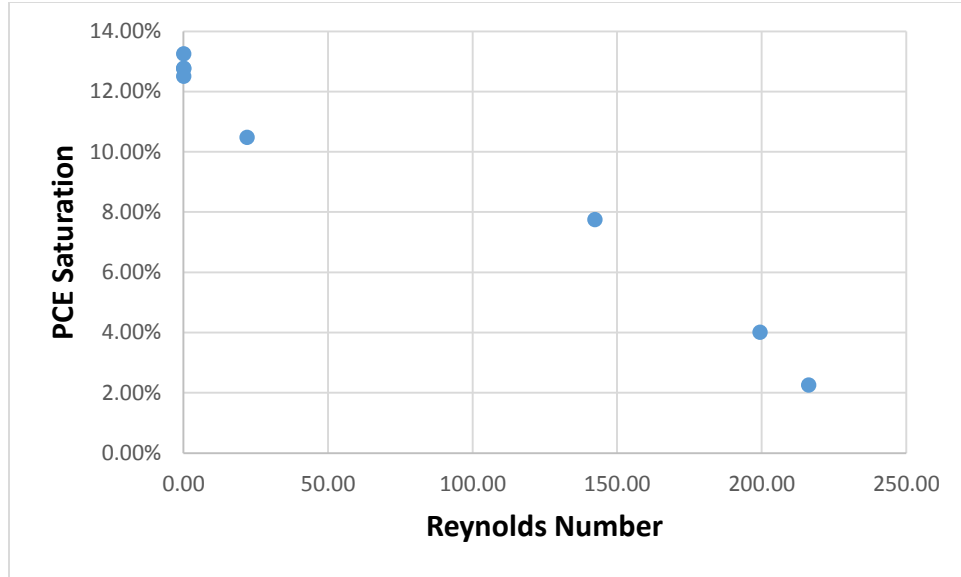


Fig 3.2: Plot of the experimental data for the uniform sand column

In the uniform sand column experiment, a near linear decrease in the residual saturation was observed as Re increased, as seen in Fig 3.2. The PCE saturation finally ended up around 2% at an Re of 220.

A problem with the uniform sand column was that the sphere packing program used to generate the medium for the lattice Boltzmann simulations was unable to precisely match the experimental column. Therefore, a column medium consisting of a polydisperse sand and glass bead mixture with a log normal grain size distribution was produced and used to pack subsequent columns as discussed in the next section.

3.2.4 High-Variance Sand Column Results

A series of PCE saturation experiments were conducted with four different columns (HV1, HV2, HV3 and HV4) packed with the same polydisperse sand and glass bead mixture with a log normal grain size distribution using three different batches of PCE. The experimental observations of the high-variance sand columns were generally similar to those of the uniform sand column.

First, a series of PCE saturation experiments were conducted on HV1, HV2 and HV3 using PCE #1. For PCE #1 in HV1, HV2 and HV3, the average initial saturations (after 20 mL/hr distilled water flushing) were $7.7 \pm 0.4\%$, $8 \pm 1\%$ and $8 \pm 2\%$ respectively. These concentrations served as the starting points for the subsequent high Re experiments.

Next, a series of PCE saturation experiments were performed on HV4 using PCE #2, which had a slightly lower IFT and higher contact angle than PCE #1. The average initial saturation was $10.7 \pm 0.8\%$. This initial residual PCE saturation of PCE #2 was higher than that of PCE #1.

Finally, a series of PCE saturation experiments were carried out on HV4 using SA-saturated PCE #3, which had significantly lower IFT and higher contact angle than PCE #1 and #2. The average initial saturation was $11.9 \pm 0.5\%$. This initial residual PCE saturation of SA-saturated PCE #3 was higher than those of both PCE #1 and PCE #2.

The experimental data of all the PCE saturation experiments are shown in Tables 3.4, and then their plots are shown in Fig 3.3, Fig 3.4 and Fig 3.5. Finally, all the plots are shown in a single figure in Fig 3.6 to provide comparison of these data.

Re	PCE saturation	Re	PCE saturation	Re	PCE saturation
PCE #1 HV1					
0.04	7.33%	0.04	7.54%	0.04	8.17%
0.04	7.52%	0.04	8.01%	113.1	6.24%
143.3	3.14%	243.2	0.99%		
PCE #1 HV2					
0.04	7.85%	0.04	8.54%	0.04	8.70%
47.4	6.25%	53.0	7.09%	102.2	6.53%
143.0	4.20%	179.0	2.56%	252.5	0.86%
PCE #1 HV3					
0.04	9.03%	0.04	7.73%	0.04	7.69%
160.2	4.17%	167.8	2.74%	203.7	1.94%
228.8	0.95%	250.0	1.43%	271.0	0.95%
PCE #2 HV4					
0.04	10.50%	0.04	10.59%	0.04	11.13%
28.3	9.46%	53.0	8.57%	76.9	6.88%
101.8	6.54%	128.6	4.14%	149.6	3.42%
172.4	2.03%	189.4	1.82%	215.4	1.08%
SA-saturated PCE #3 HV4					
0.04	11.56%	0.04	11.83%	0.04	11.92%
0.04	12.37%	29.0	10.36%	30.2	10.38%
58.9	9.46%	73.5	7.73%	82.4	7.60%
98.9	5.47%	123.4	4.09%	131.2	4.18%
138.6	2.35%	153.4	1.91%	155.4	1.74%
170.7	1.59%	174.0	1.67%	191.2	1.28%
214.7	0.80%	223.3	0.79%		

Table 3.4: Experimental data of all PCE saturation experiments

All PCE #1 experimental data, grouped by different columns, are shown below in Fig 3.3. As seen in Fig 3.3, the saturation of PCE #1 decreased roughly linearly through an Re of 250, but the saturation data showed a relatively high variability at low Re regime.

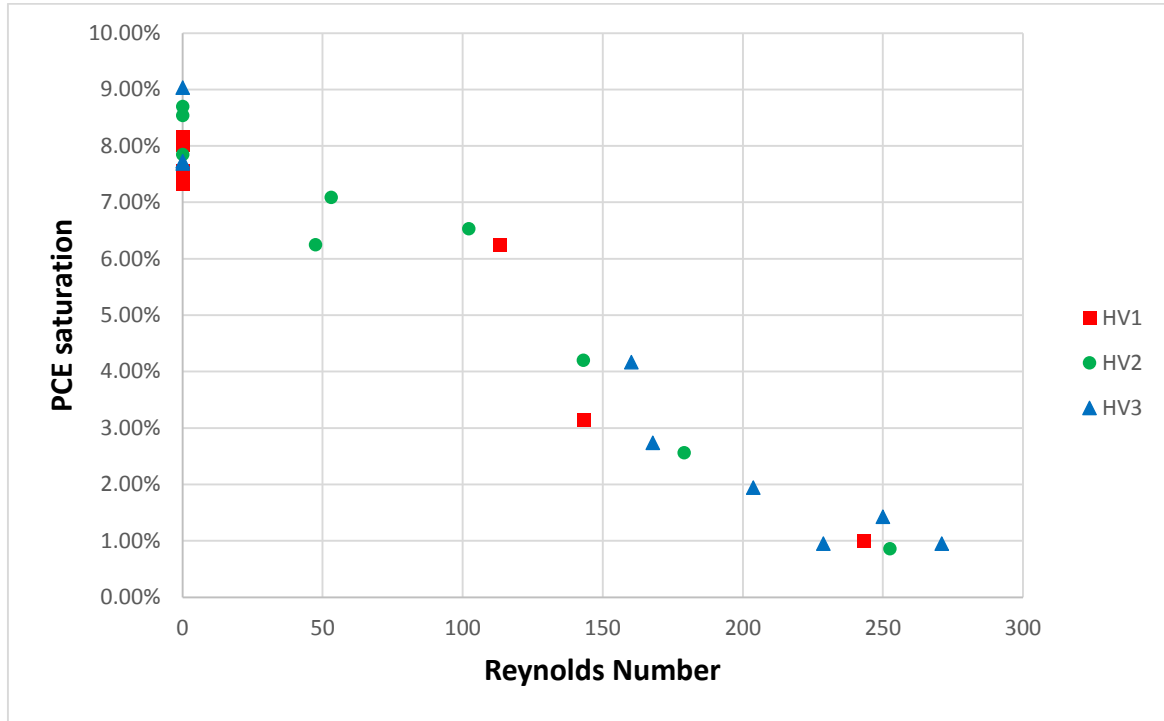


Fig 3.3: Plot of the experimental data of HV1, HV2 and HV3 using PCE #1

For the experiments conducted with PCE #2, the PCE saturation decreased almost linearly as Re was increased to about 225, as seen in Fig 3.4. The PCE saturations of PCE #2 were considerably higher than those of PCE #1 (Fig 3.3) in the low Re regime, however, the differences between PCE #1 and PCE #2 saturations began to decrease as Re increased. The saturations for both PCE #1 and PCE #2 were around 1% at $Re > 220$.

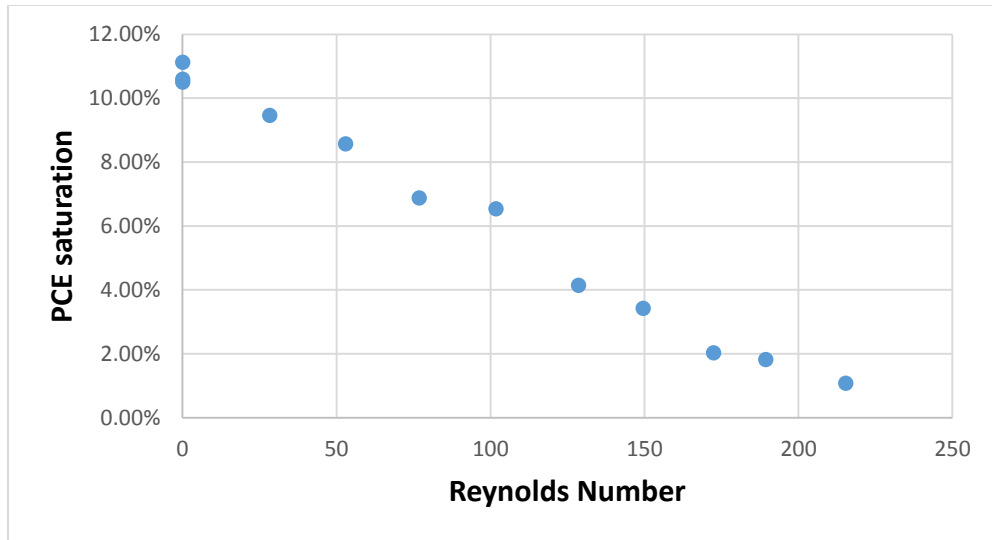


Fig 3.4: Plot of the experimental data of HV4 using PCE #2

The plot of SA-saturated PCE #3 shown below in Fig 3.5 resembles a hockey stick. The saturation of SA-saturated PCE #3 decreased roughly linearly through an Re of 150, then the trend became much flatter through an Re of 220. SA-saturated PCE #3 displayed higher saturations relative to prior two batches of PCE in the low Re regime, and the differences began to decrease as Re increased. The saturation of SA-saturated PCE #3 was around 0.8% at an Re of 220, which was very close to PCE #1 and PCE #2.

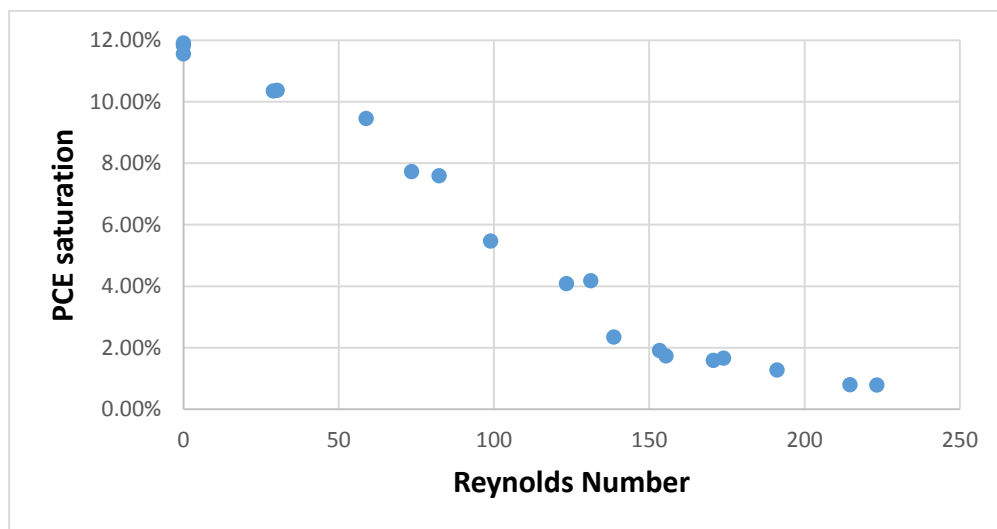


Fig 3.5: Plot of the experimental data of HV4 using SA-saturated PCE #3

Fig 3.6 shows all the plots in a single picture, where all the initial saturations were averaged to show only one starting point.

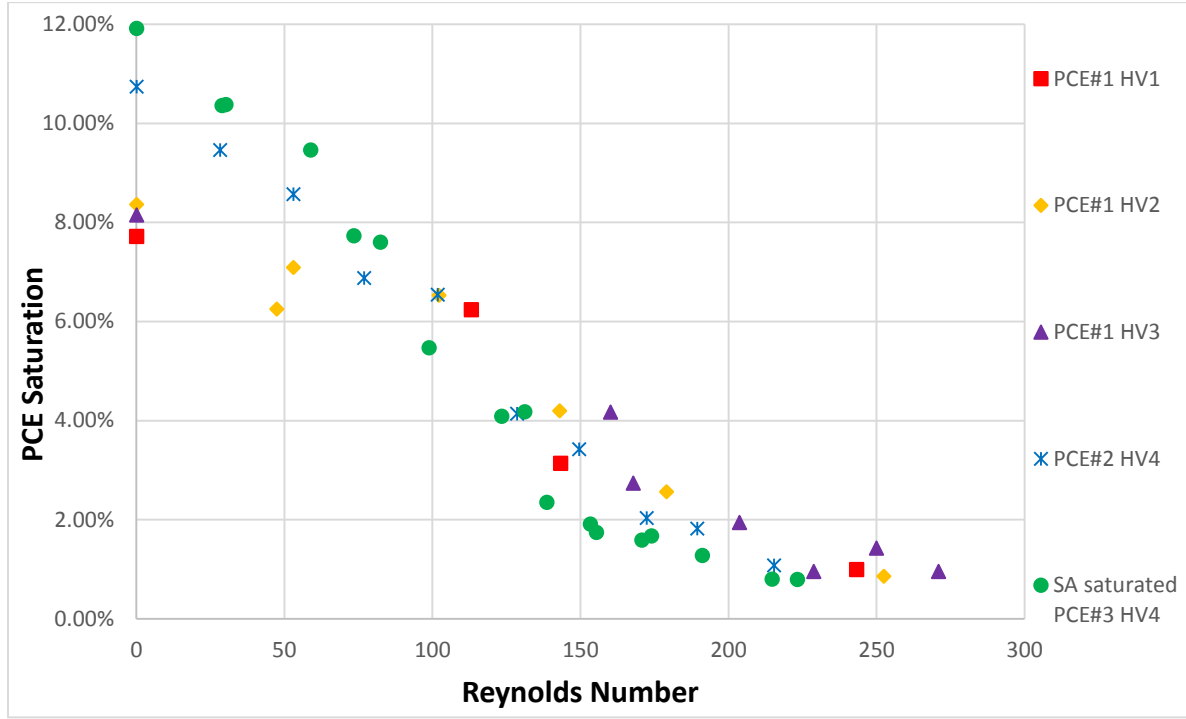


Fig 3.6: Plot of the experimental data of all columns using different PCE

3.3 Lattice Boltzmann Results

Lattice Boltzmann simulations were conducted for a system corresponding to the high-variance sand columns to compare with experimental results. Since there was a discrepancy between the initial conditions of experimental data and those of simulation data, the saturation data were normalized by the initial residual saturation in order to make their initial conditions match. The simulated NWP saturations were always greater than the experimental data so the saturation data was normalized based on the initial residual saturation of simulated data.

The entrapped non-wetting phase saturation for each synthetic porous medium system is listed in Table 3.6, relevant plots are shown in Fig 3.7, Fig 3.8, Fig 3.9, Fig 3.10, Fig 3.11 and Fig 3.12. The upper limit of Re was 220.0 because when $Re > 220$, the flow was transitioning to

turbulent flow and the pressure and velocity in the system became constantly oscillating, such that a steady state flow field could not be achieved. To capture all the physics in this regime, the system needs to be discretized even more and due to limited computing power that becomes difficult.

Re	PCE saturation	Normalized	Re	PCE saturation	Normalized
PCE #1					
0.04	10.72%	100%	5.0	10.54%	98.32%
35.0	9.17%	85.54%	60.0	8.18%	76.31%
100.0	6.42%	59.89%	150.0	4.74%	44.22%
180.0	3.84%	35.82%	200.0	3.23%	30.13%
220.0	2.77%	25.84%			
PCE #2					
0.04	11.81%	100%	5.0	11.59%	98.14%
35.0	10.23%	86.62%	60.0	9.16%	77.56%
100.0	7.02%	59.44%	150.0	4.16%	35.22%
180.0	2.57%	21.76%	200.0	2.17%	18.37%
220.0	2.01%	17.02%			
SA-saturated PCE #3					
0.04	13.62%	100%	5.0	13.38%	98.24%
35.0	11.74%	86.20%	60.0	10.22%	75.04%
100.0	7.81%	57.34%	150.0	4.62%	33.92%
180.0	3.13%	22.98%	200.0	2.63%	19.31%
220.0	2.47%	18.14%			

Table 3.5: Lattice Boltzmann simulation data

A plot including both experimental and simulation data of PCE #1 is shown below in Fig 3.7, followed by a plot of the normalized data in Fig 3.8 where the raw data in Fig 3.7 have been shifted down after normalizing. In general, when $Re < 220$, simulation data of PCE #1 decreased linearly as Re increased.

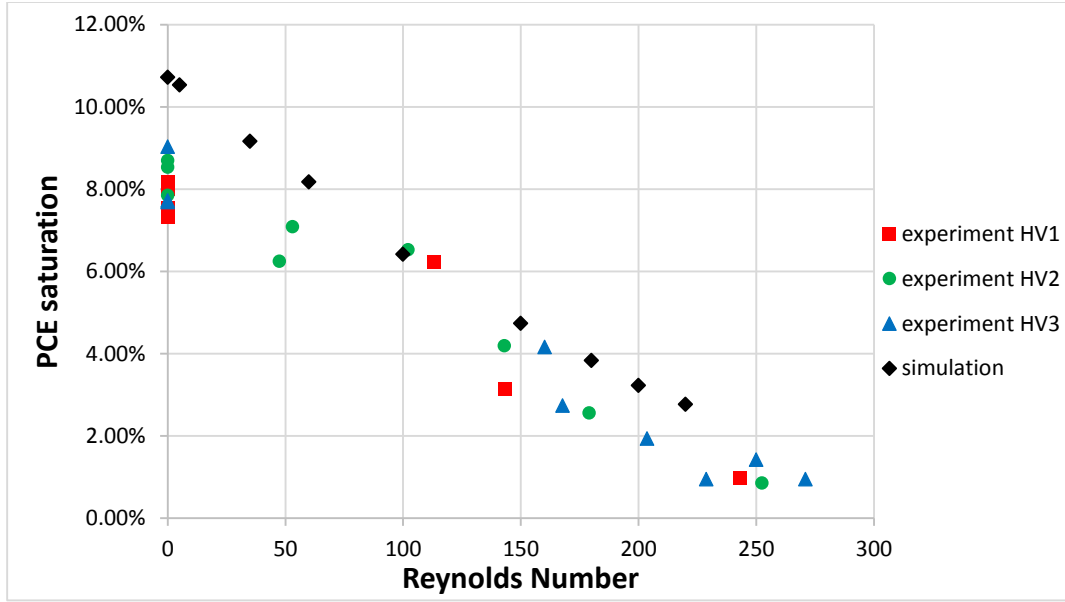


Fig 3.7: Plot of experimental and simulation data of PCE #1

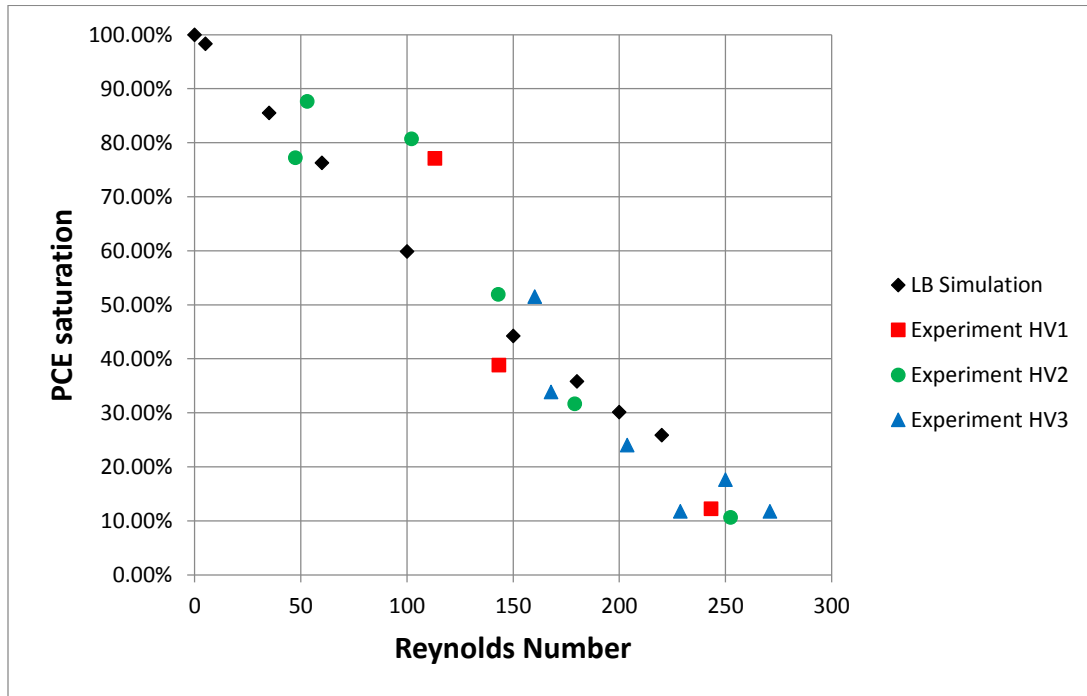


Fig 3.8: Plot of normalized experimental and simulation data of PCE #1

A plot of experimental and simulation data of PCE #2 is shown below in Fig 3.9, followed by a plot of normalized data shown in Fig 3.10. As is expected, simulated residual saturations of PCE #2 were higher than those of PCE #1.

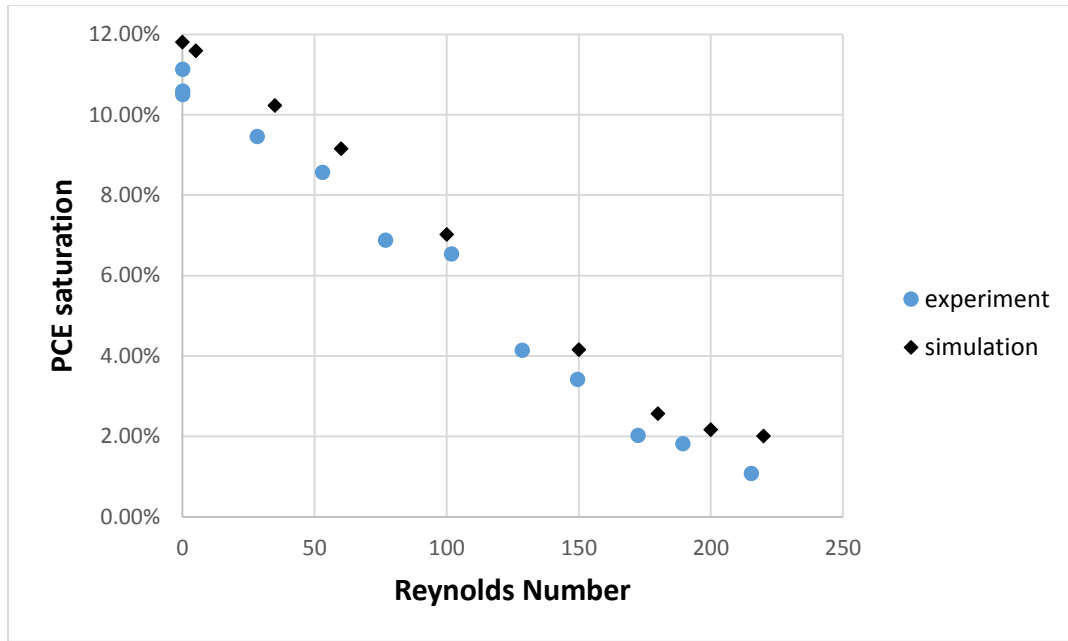


Fig 3.9: Plot of experimental and simulation data of PCE #2

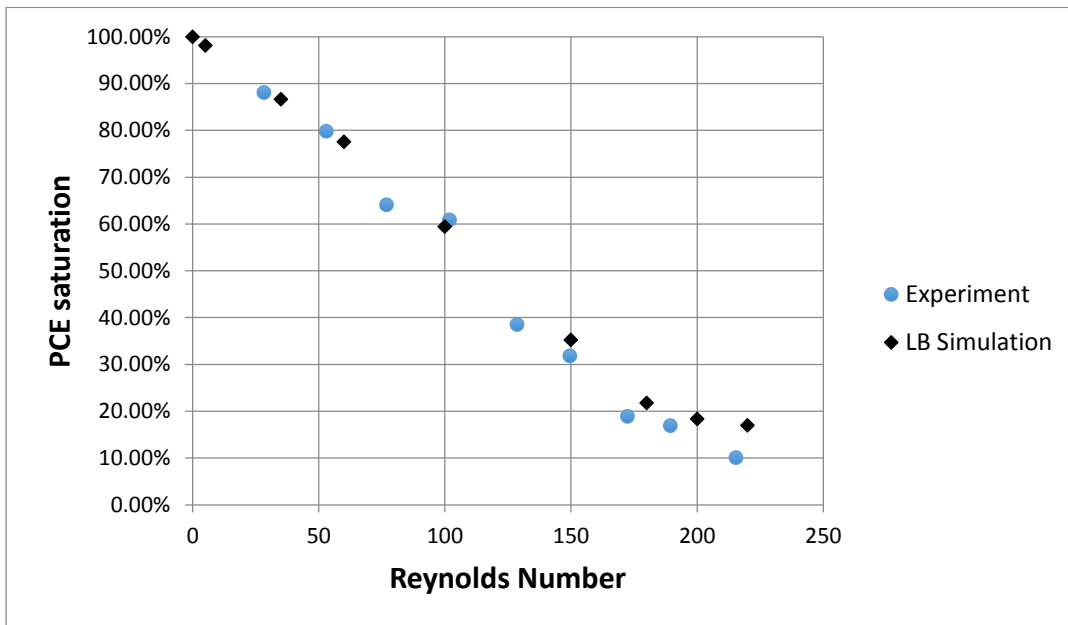


Fig 3.10: Plot of normalized experimental and simulation data of PCE #2

According to Fig 3.9 and Fig 3.10, the simulation data of PCE #2 matched the experimental data much better than those of PCE #1. Similarly, simulation data decreased linearly as Re was increased to 180, then the trend became much flatter through an Re of 220.

A plot of experimental and simulation data of SA-saturated PCE #3 is shown below in Fig 3.11, followed by a plot of normalized data shown in Fig 3.12. Similar to PCE #2, simulation data of SA-saturated PCE #3 decreased linearly through an Re of 180, then the trend became much flatter through an Re of 220.

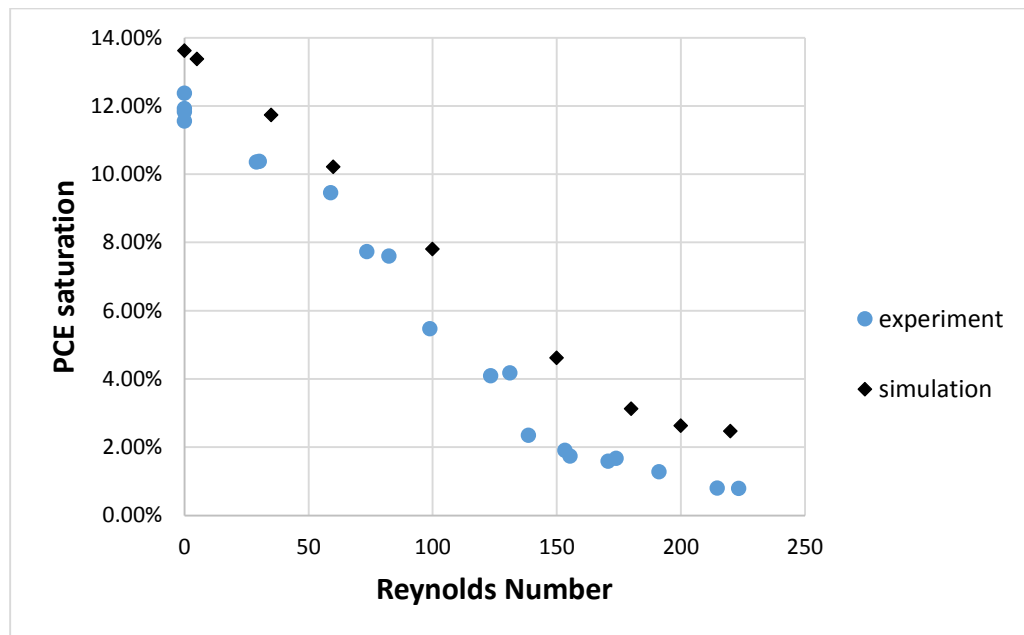


Fig 3.11: Plot of experimental and simulation data of SA saturated PCE #3

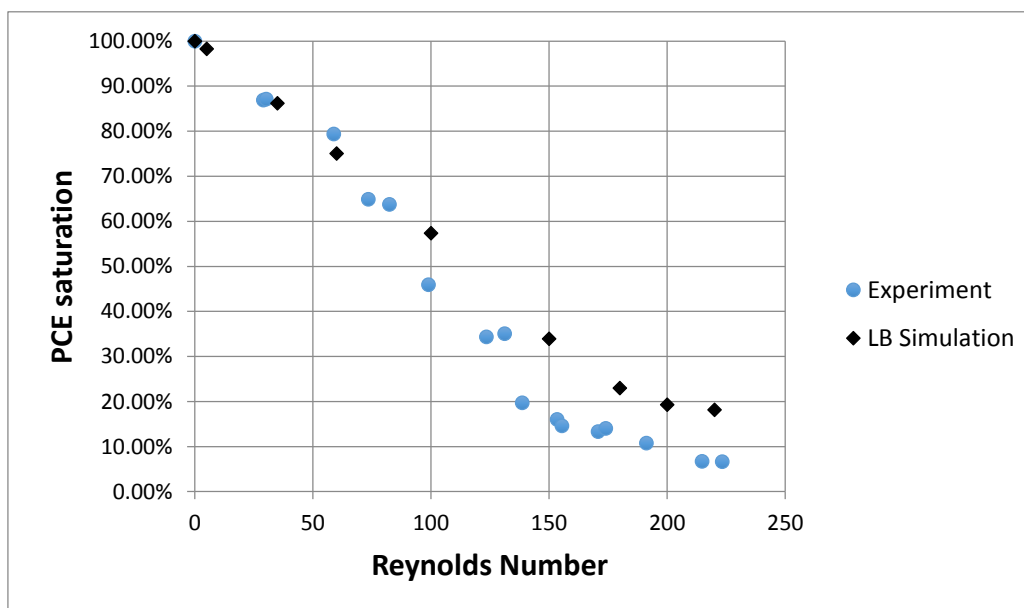


Fig 3.12: Plot of normalized experimental and simulation data of SA saturated PCE #3

Overall, all simulation data decreased linearly through an Re of 180. Then, simulation data of PCE #2 and SA saturated PCE #3 became much flatter, resulting in a hockey-stick shape, which was however, not obvious for the results using PCE #1. Among all three batches of PCE, simulation data of PCE #2 most closely matched the experimental data.

CHAPTER 4: DISCUSSIONS

4.1 NAPL Mobilization Mechanisms

Before the experimental results are analyzed and discussed, NAPL mobilization mechanisms, from which the expressions of three significant dimensionless quantities (N_{Ca} , N_B and N_T) are derived, needs to be introduced.

In order to analyze NAPL mobilization mechanism, it is reasonable to start from a single NAPL droplet entrapped in a single pore in porous media. Fig 4.1 depicts a single NAPL droplet stuck in a pore volume. In the 2D slide, NAPL is depicted in color and the porous media is in black. In the 3D rendering, the red spheres represent the porous media and the green one represents the NAPL.

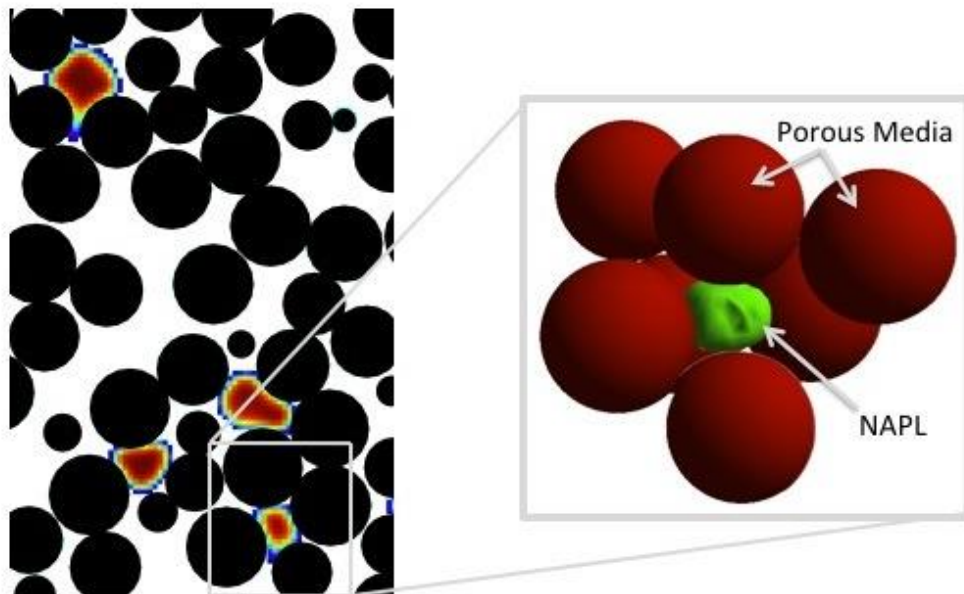


Fig 4.1: NAPL entrapped in porous media. At left, a 2D image of NAPL droplets in a porous medium system. At right, a 3D representation of a single NAPL droplet.

When a NAPL droplet is entrapped in a single pore in porous media, it is actually in a state of force balance within this pore, which is formally termed as the critical conditions for mobilization. Under such conditions, mobilization forces balance retention forces. More specifically, viscous and gravity/buoyancy forces acting to mobilize the NAPL droplet, are balanced by capillary forces acting to retain the NAPL droplet.

By equating the balanced forces in the critical conditions and applying Darcy's law to express the pressure gradient, Pennell et al. (1996) proved that the expression $N_{Ca} + N_B \sin \alpha$ could be used to assess the potential for NAPL mobilization in a pore [33], where $N_{Ca} = \frac{q_w \mu_w}{\sigma_{ow} \cos \theta}$ which represents the ratio of the viscous to capillary forces, $N_B = \frac{\Delta \rho g k k_{rw}}{\sigma_{ow} \cos \theta}$ which represents the ratio of the gravity/buoyancy to capillary forces, α is the angle the flow makes with the positive x axis. N_{Ca} and N_B are used to quantify the contribution of viscous and gravity/buoyancy forces to NAPL mobilization respectively, although alternative expressions for them exist [84, 85, 86, 87, 88, 89, 90], their functionalities remain unchanged.

The combined effect of N_{Ca} and N_B is represented by N_T and is expressed as [33]:

$$N_T = \sqrt{N_{Ca}^2 + 2N_{Ca}N_B \sin \alpha + N_B^2}$$

By following the convention above for N_{Ca} and N_B , for vertical flow ($\alpha = 90^\circ$), in the direction of the buoyancy force, the expression for N_T becomes [33]:

$$N_T = \sqrt{N_{Ca}^2 + 2N_{Ca}N_B + N_B^2} = |N_{Ca} + N_B| = \left| \frac{q_w \mu_w + \Delta \rho g k k_{rw}}{\sigma_{ow} \cos \theta} \right|$$

This expression suggests that at low flow rates when N_T is relatively small, NAPL droplets are trapped in the porous media by capillary force, whereas at high flow rate when N_T is relatively large, capillary forces are overwhelmed by the viscous forces, which act to mobilize the droplet.

4.2 Comparison of Simulation and Experimental Results

First, the discrepancy between the simulation and experimental results must be addressed. It has already been shown in Section 3.3 that simulation data were always larger than experimental data, which can be observed from the initial residual saturation through the saturation under the upper limit of Re . This actually results from the fact that the simulated system, as presented in Section 2.3.4, was only an idealized representation of the experimental porous media rather than a realistic picture of the actual porous media. Therefore, it is reasonable to see the simulation and experimental results were not exactly same.

Next, the relationship between saturations and N_T will be examined based on the theory described in Section 4.1. Data were obtained from column experiments and simulation results, plots were made with both normalized saturations and absolute ones. All the N_{Ca} , N_B and N_T results for both experiments and simulations are shown below in Table 4.1 and Table 4.2 respectively, and plots are shown in Fig 4.2, Fig 4.3, Fig 4.4 and Fig 4.5. The physical and chemical constants used in computing are listed as follows: the density of water: $0.998 \text{ g}\cdot\text{cm}^{-3}$ (22.0°C), the density of PCE: $1.623 \text{ g}\cdot\text{cm}^{-3}$ (20°C), μ_w : $0.890 \text{ mPa}\cdot\text{s}$ (25°C) [80], gravity acceleration constant: $9.8 \text{ m}\cdot\text{s}^{-2}$, k : $1.4\times 10^{-10} \text{ m}^2$ and k_{rw} : 0.7. θ_s was used to represent the contact angle.

Re	Darcy velocity (m/s)	N_{Ca}	N_T	PCE saturation	Normalized saturation
PCE #1 ($N_B = -1.93\text{E-}5$)					
0.04	0.00001	3.07E-7	1.90E-5	8.07%	100%
47.4	0.01239	3.55E-4	3.36E-4	6.25%	77.45%

53.0	0.01386	3.97E-4	3.78E-4	7.09%	87.86%
102.2	0.02672	7.66E-4	7.47E-4	6.53%	80.92%
113.1	0.02975	8.53E-4	8.34E-4	6.24%	77.32%
143.0	0.03739	1.07E-3	1.05E-3	4.20%	52.04%
143.3	0.03769	1.08E-3	1.06E-3	3.14%	38.91%
160.2	0.04464	1.28E-3	1.26E-3	4.17%	51.65%
167.8	0.04676	1.34E-3	1.32E-3	2.74%	33.94%
179.0	0.04680	1.34E-3	1.32E-3	2.56%	31.72%
203.7	0.05676	1.63E-3	1.61E-3	1.94%	24.07%
228.8	0.06376	1.83E-3	1.81E-3	0.95%	11.79%
243.2	0.06396	1.83E-3	1.82E-3	0.99%	12.27%
250.0	0.06966	2.00E-3	1.98E-3	1.43%	17.67%
252.5	0.06601	1.89E-3	1.87E-3	0.86%	10.66%
271.0	0.07552	2.17E-3	2.15E-3	0.95%	11.79%
PCE #2 ($N_B = -2.32E-5$)					
0.04	0.00001	4.12E-7	2.28E-5	10.74%	100%
28.3	0.00848	2.92E-4	2.68E-4	9.46%	88.08%
53.0	0.01589	5.46E-4	5.23E-4	8.57%	79.80%
76.9	0.02305	7.92E-4	7.69E-4	6.88%	64.06%
101.8	0.03052	1.05E-3	1.03E-3	6.54%	60.89%
128.6	0.03855	1.33E-3	1.30E-3	4.14%	38.54%
149.6	0.04485	1.54E-3	1.52E-3	3.42%	31.84%
172.4	0.05168	1.78E-3	1.75E-3	2.03%	18.90%
189.4	0.05678	1.95E-3	1.93E-3	1.82%	16.95%
215.4	0.06458	2.22E-3	2.20E-3	1.08%	10.06%
PCE #3 ($N_B = -6.75E-5$)					
0.04	0.00001	1.20E-6	6.63E-5	11.92%	100%
29.0	0.00869	8.70E-4	8.03E-4	10.36%	86.91%
30.2	0.00905	9.06E-4	8.39E-4	10.38%	87.08%
58.9	0.01766	1.77E-3	1.70E-3	9.46%	79.36%

73.5	0.02203	2.21E-3	2.14E-3	7.73%	64.85%
82.4	0.02470	2.47E-3	2.40E-3	7.60%	63.76%
98.9	0.02965	2.97E-3	2.90E-3	5.47%	45.89%
123.4	0.03699	3.70E-3	3.64E-3	4.09%	34.31%
131.2	0.03933	3.94E-3	3.87E-3	4.18%	35.07%
138.6	0.04155	4.16E-3	4.09E-3	2.35%	19.71%
153.4	0.04599	4.60E-3	4.54E-3	1.91%	16.02%
155.4	0.04659	4.66E-3	4.60E-3	1.74%	14.60%
170.7	0.05117	5.12E-3	5.05E-3	1.59%	13.34%
174.0	0.05216	5.22E-3	5.15E-3	1.67%	14.01%
191.2	0.05732	5.74E-3	5.67E-3	1.28%	10.74%
214.7	0.06437	6.44E-3	6.37E-3	0.80%	6.71%
223.3	0.06694	6.70E-3	6.63E-3	0.79%	6.63%

Table 4.1: N_{Ca} , N_B and N_T for each PCE saturation experiment

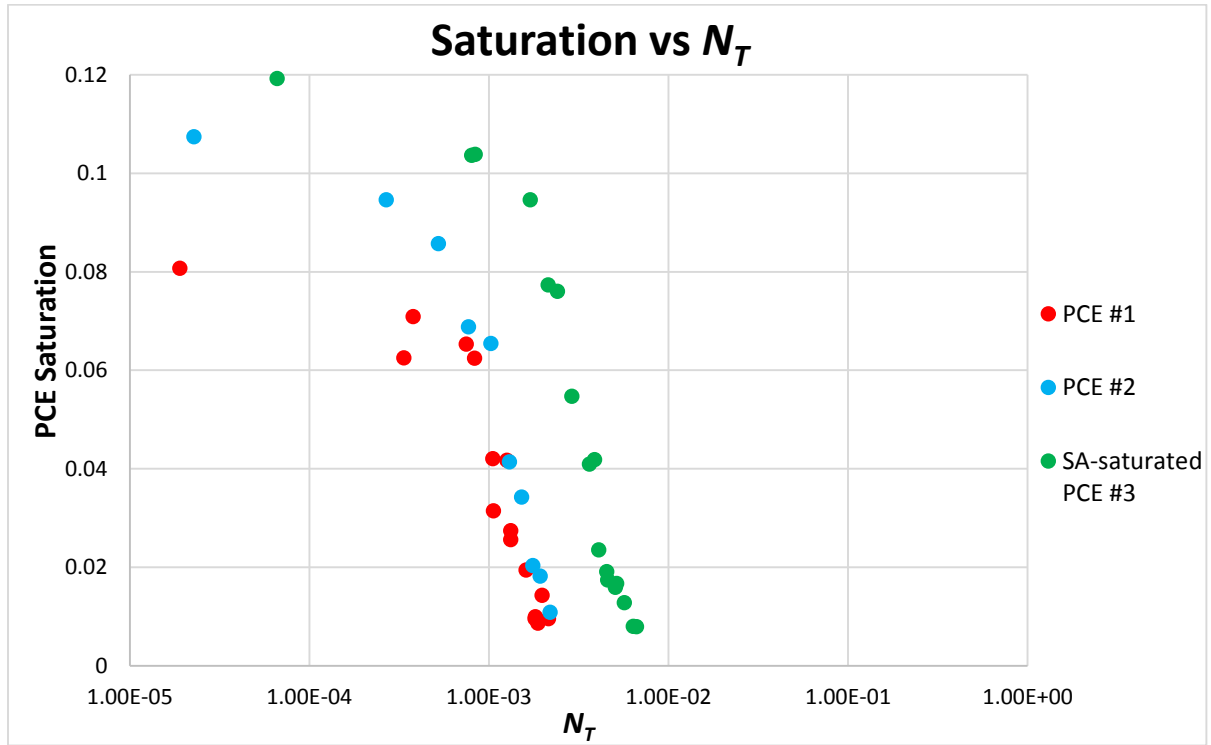


Fig 4.2: Plot of saturation (non-normalized) vs N_T for experiments

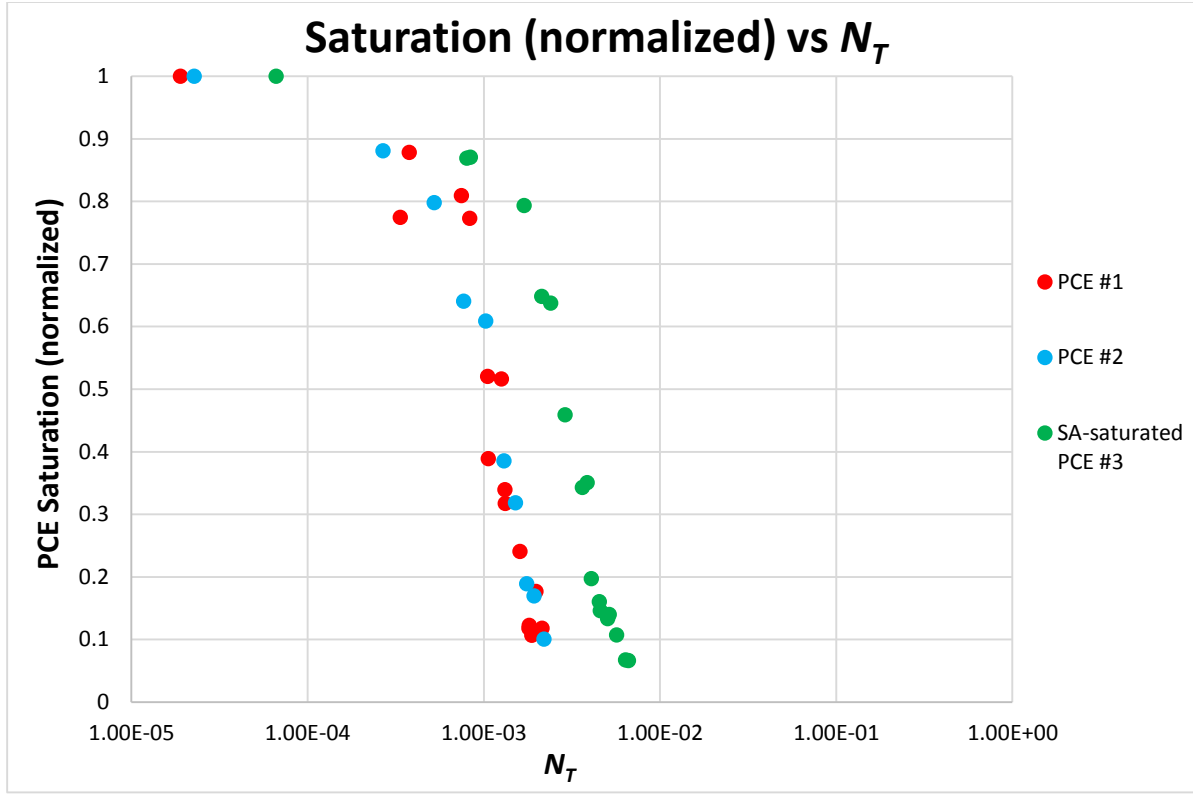


Fig 4.3: Plot of saturation (normalized) vs N_T for experiments

Re	Darcy velocity (m/s)	N_{Ca}	N_T	PCE saturation	Normalized saturation
PCE #1 ($N_B = -1.93E-5$)					
0.04	0.00001	3.05E-7	1.90E-5	10.72%	100%
5.0	0.00133	3.82E-5	1.88E-5	10.54%	98.32%
35.0	0.00931	2.67E-4	2.48E-4	9.17%	85.54%
60.0	0.01597	4.58E-4	4.39E-4	8.18%	76.31%
100.0	0.02661	7.63E-4	7.44E-4	6.42%	59.89%
150.0	0.03992	1.14E-3	1.13E-3	4.74%	44.22%
180.0	0.04790	1.37E-3	1.35E-3	3.84%	35.82%
200.0	0.05323	1.53E-3	1.51E-3	3.23%	30.13%
220.0	0.05855	1.68E-3	1.66E-3	2.77%	25.84%
PCE #2 ($N_B = -2.32E-5$)					
0.04	0.00001	3.66E-7	2.28E-5	11.81%	100%
5.0	0.00133	4.57E-5	2.26E-5	11.59%	98.14%

35.0	0.00931	3.20E-4	2.97E-4	10.23%	86.62%
60.0	0.01597	5.49E-4	5.26E-4	9.16%	77.56%
100.0	0.02661	9.15E-4	8.91E-4	7.02%	59.44%
150.0	0.03992	1.37E-3	1.35E-3	4.16%	35.22%
180.0	0.04790	1.65E-3	1.62E-3	2.57%	21.76%
200.0	0.05323	1.83E-3	1.81E-3	2.17%	18.37%
220.0	0.05855	2.01E-3	1.99E-3	2.01%	17.02%
PCE #3 ($N_B = -6.75E-5$)					
0.04	0.00001	1.07E-6	6.64E-5	13.62%	100%
29.0	0.00133	1.33E-4	6.57E-5	13.38%	98.24%
30.2	0.00931	9.32E-4	8.65E-4	11.74%	86.20%
58.9	0.01597	1.60E-3	1.53E-3	10.22%	75.04%
73.5	0.02661	2.66E-3	2.60E-3	7.81%	57.34%
82.4	0.03992	4.00E-3	3.93E-3	4.62%	33.92%
98.9	0.04790	4.79E-3	4.73E-3	3.13%	22.98%
123.4	0.05323	5.33E-3	5.26E-3	2.63%	19.31%
131.2	0.05855	5.86E-3	5.79E-3	2.47%	18.14%

Table 4.2: N_{Ca} , N_B and N_T for each PCE saturation simulation

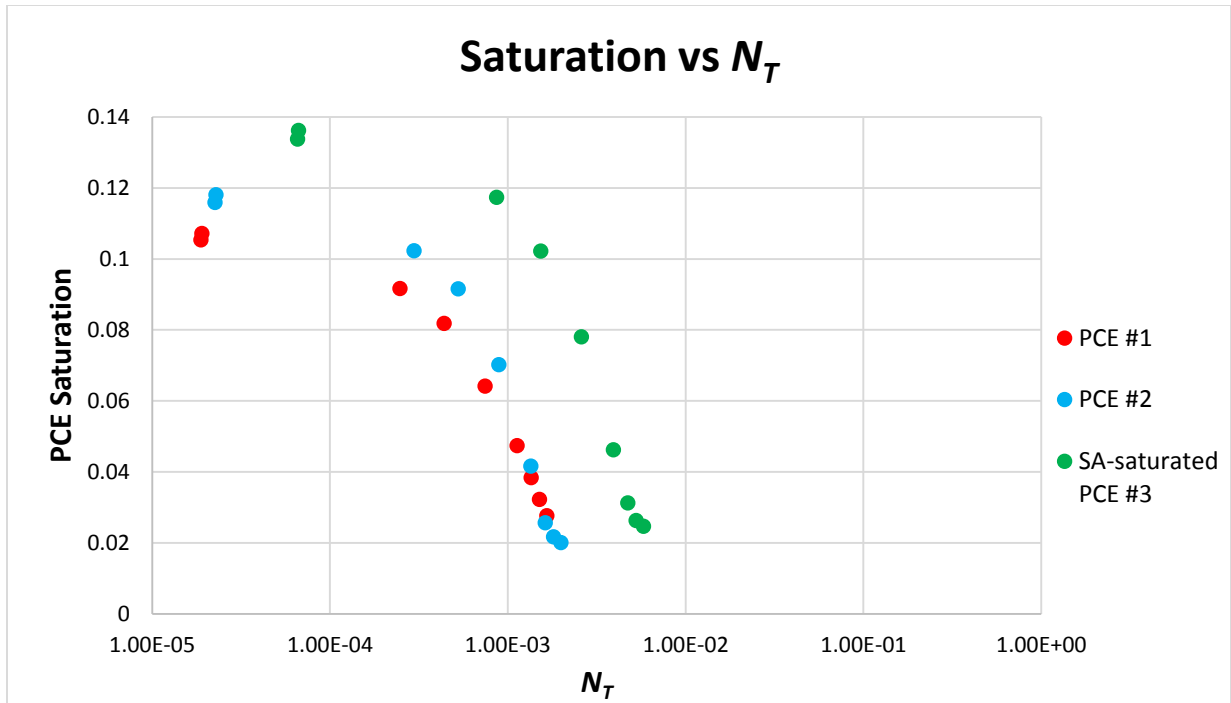


Fig 4.4: Plot of saturation (non-normalized) vs N_T for simulation

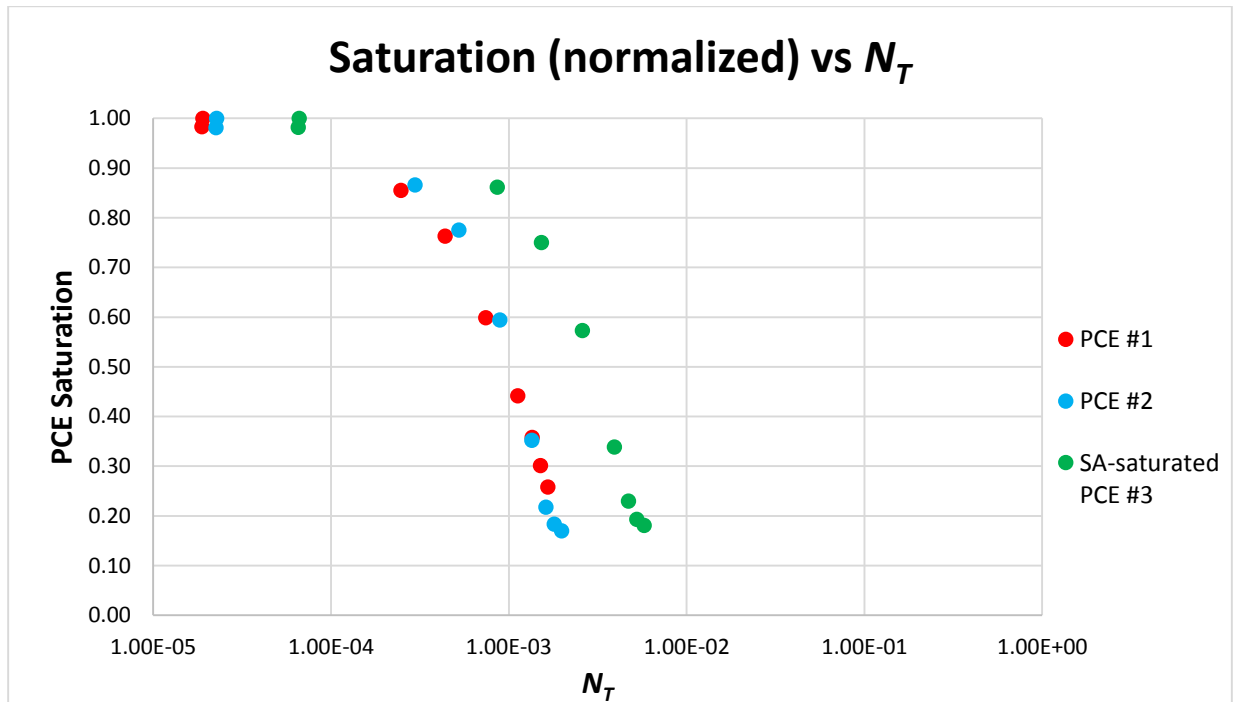


Fig 4.5: Plot of saturation (normalized) vs N_T for simulation

Based on the plots above, simulation and experimental results were generally in the same pattern, where the PCE #1 and PCE #2 data very closely fall on top of each other, while SA-saturated PCE #3 is shifted to the right. The plots show that the residual saturation was generally a decreasing function of the N_T for each batch of PCE, which implies N_T correlated reasonably well with the residual PCE saturation. However, N_T failed to predict the differences in saturation in different batches of PCE. It is obvious that SA-saturated PCE #3 requires a larger N_T than PCE #1 and PCE #2 to remove the same amount of PCE.

Pennell et al. (1996) obtained the critical values of N_T for PCE mobilization in sand columns, which was reported to be around 10^{-5} for initial mobilization and more than 10^{-3} for complete removal [33]. This result has been validated by Li et al. (2007), Boving et al. (2000) and Linda et al. (2008) using various NAPL and porous media [36, 91, 93]. Zhang et al. (2008) investigated the critical N_T for various size fractions of Accusand using 1,3,5-Trifluorobenzene as the DNAPL. For the 12/20 mesh size, N_T was found to be more than 10^{-6} for initial mobilization and almost 10^{-3} for complete removal [46]. Taylor et al. (2004) observed that a N_T around 10^{-5} results in about 11% PCE saturation in 20-30 mesh sand columns [55]. These results are generally in good agreement with the experimental results in this study.

The experimental results were reinforced by the simulation results, which displayed a consistent pattern. The unique feature of SA-saturated PCE #3 is probably due to the distinct properties of the SA-saturated PCE #3. According to the fluid properties of three batches of PCE presented in Section 3.1.2. SA-saturated PCE #3 displayed a stronger wettability compared to other two batches of PCE. The measured IFT values were similar for PCE #1 and PCE #2 (37 and 36 mN/m, respectively), and significantly lower for the SA-saturated PCE #3 (26 mN/m). The θ_s of SA-saturated PCE #3 (70°) was more than twice that of PCE#1 (33°) and more than

1.5 times that of PCE #2 (44°), respectively. Since IFT and contact angles are important properties that have been proven to affect NAPL mobilization, and other quantities (i.e., μ_w , $\Delta\rho$, g , k , and k_{rw}) were considered as constants when computing, it is reasonable to make assumption that possible causes of this shift were the differences in IFT and wettability. G.C. Tzimas et al. (1997) also found that wettability affects the mechanism and the efficiency of displacement significantly, especially at low capillary numbers ($N_{Ca} \leq 10^{-6}$). The saturation increased as the wettability increased [81], which is consistent with the fact that SA-saturated PCE #3 was present at the highest residual saturations at low flow rates, instead of the lowest residual saturations as predicted by N_T . Zheng and Powers (2003) stated that reducing the IFT would allow a DNAPL to enter smaller pores that may be less readily accessible during remediation efforts [76]. The deviation of SA-saturated PCE #3 from PCE #1 and PCE #2 has implied that N_T has shortcomings and limitations as a tool to assess NAPL mobilization, which will be discussed in detail in Section 4.3.

Turbulence phenomena occurred at high flow rates in the study, and at higher flow rate turbulent flow became more apparent in the simulated system. Fig 4.6 highlights the turbulence in the simulated system. This is a region taken from the medium during a flow at an Re of 220. The green area represents the porous media and the colorful features represent the PCE that was entrapped in the pores.

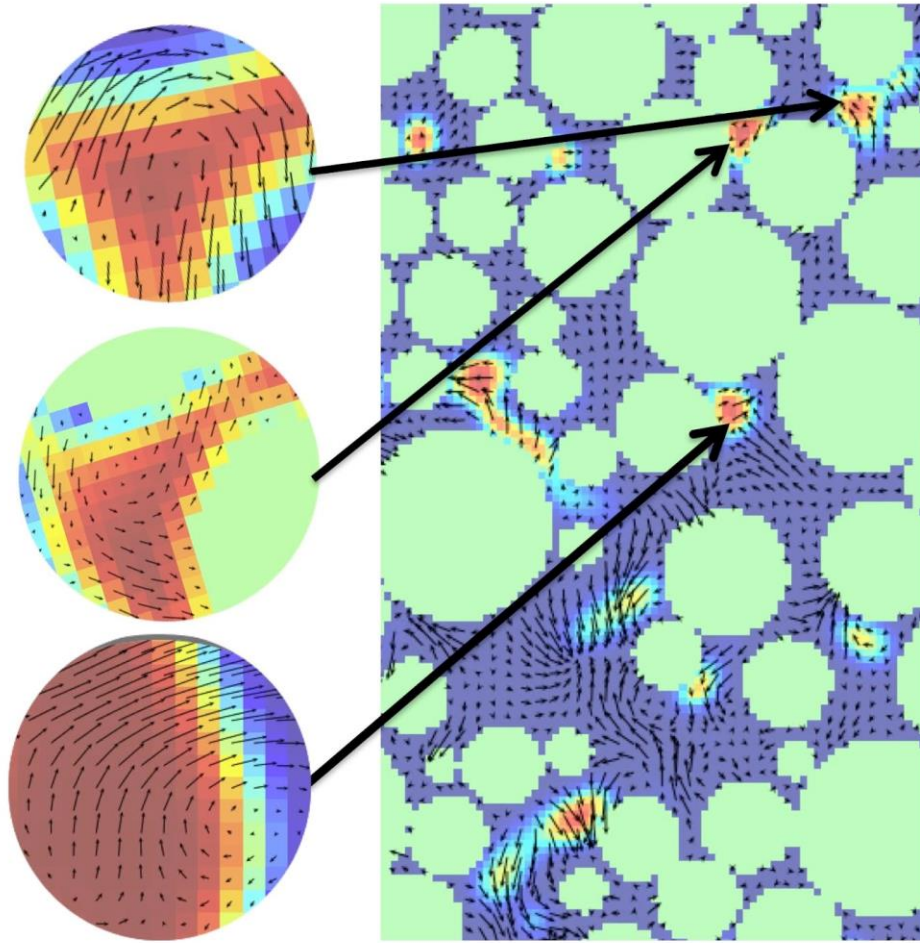


Fig 4.6: Turbulence in the simulated system at an Re of 220

Based on the experimental and simulation results as well as their plots, there is evidence to suggest that turbulence could impact PCE mobilization at flow rates higher than an Re of 180, flattening the decreasing of PCE mobilization as the Re increases to form a hockey stick shape. However, based on the data set it is not clear what role of turbulence was during the High Re flushing. Further investigation on the effect of turbulence on NAPL mobilization is needed.

4.3 Significance of Findings

We note that N_T has shortcomings and limitations as a tool to assess NAPL mobilization in Section 4.2. In fact, similar findings have also been reported in several previous studies. Duffield et al. (2003) found that N_T was not accurate especially for systems where free product NAPL was

present, and the limitations in this case were believed to result from the formation and transport of macro-emulsions [94]. Padgett et al. (1999) observed that residual PCE began to mobilize in the clay-mixed media at a range of N_T below those reported in the literature for homogeneous well-sorted sand [96]. The fact that different porous media could result in different critical N_T value was also widely reported in other studies [33, 36, 77, 56, 55, 46, 38]. Conrad et al. (2002) concluded three factors that might cause the departures between the assumptions contained within N_T analysis and the situation seen in the experiments, which are: (1) the N_T analysis ideally considers NAPL trapped in the pore in porous media as a blob, instead of a large, continuous free phase NAPL; (2) N_T is derived in a homogeneous system, instead of a real, heterogeneous system; (3) N_T analysis assumes that IFT remains spatially constant, which is not always true for cases where surfactants are used [31].

In conclusion, based on the experimental results, N_T correlated reasonably well with the residual PCE saturation, however, it did not work as a predictive model. N_T was not the only determinative factor in our NAPL mobilization experiments because of the following reasons:

(1) It does not account for different initial NAPL distributions in different systems;

(2) It does not account for geometrical considerations (e.g. different drop shapes due to different wettabilities and/or initial distributions, or complex topology and morphology of the porous media); and

(3) It does not account for the viscosity of the NAPL phase (which could vary between the SA-saturated PCE and other PCEs). The impact of viscosity on the residual saturation has been reported by G.C. Tzimas et al. (1997) [81].

CHAPTER 5: CONCLUSIONS

Groundwater is one of the nation's most important natural resources, composing about 30% of total freshwater [4]. Approximately 44% of the U.S. population depends on groundwater for its drinking water supply [27]. However, groundwater is subject to contamination, which can be very difficult and expensive to remove.

In groundwater, NAPLs form a visible, separate oily phase whose migration is governed by viscous and gravity/buoyancy forces acting to mobilize the NAPL droplet, and capillary forces acting to retain the NAPL droplet. The flow rate used to mobilize the NAPL droplet, the density difference between the NAPL and the aqueous phase, and the IFT between the NAPL and the aqueous phase together with the wettability of the NAPL due to the aqueous phase are main controllers that affect viscous, gravity/buoyancy, and capillary forces respectively. In order to quantify the effects of these forces, three dimensionless numbers have been introduced: (1) N_{Ca} which represents the ratio of viscous forces to capillary forces, (2) N_B which represents the ratio of the gravity/buoyancy to capillary forces, and (3) N_T which represents the overall ratio of mobilizing forces to trapping forces. N_T has been used as a criterion to predict the onset and extent of residual NAPL mobilization in porous media in many previous studies.

Column experiments have been conducted to investigate experimentally the effect of viscous forces in mobilizing entrapped NAPL by varying the flow rate. Based on the experimental results, the residual NAPL saturations decreased roughly linearly as the viscous forces increased. In the residual saturation experiments, N_{Ca} was always the main contributor to the N_T , which

means the viscous forces increasingly overwhelmed the capillary forces and the gravity/buoyancy forces were less important to the viscous forces in these experiments.

The IFT and contact angle have been found to affect the NAPL mobilization. The initial residual saturation was observed to increase as the wettability increased, which is probably due to the fact that a lower IFT and higher contact angle would allow a NAPL droplet to enter smaller pores that may be less readily accessible during aqueous phase flushing. Therefore, the series of experiments potentially started with different NAPL saturations and a different distribution of that NAPL in the pore space. At low flow rates, this phenomenon was important, whereas at higher flow rates, the viscous forces began to dominate to an extent that the NAPL properties became much less important, this explains why there was no obvious difference between the residual saturations of different batches of PCE at a relatively high Re .

The experimental results indicate that N_T correlated reasonably well with the residual NAPL saturation. However, the discrepancy of residual saturation versus N_T among different batches of PCE has implied some shortcomings and limitations of N_T as a tool to assess the NAPL residual saturation. Other factors appear to be important when predicting the residual saturation of entrapped NAPL. For example, the morphology and topology of the pore space is certainly important, and the wettability of the NAPL to the aqueous phase may affect the mechanism and the efficiency of displacement significantly. These mechanisms are not included or incompletely included in N_T analysis. Therefore, it is reasonable to conclude that N_T is not a complete measure of the many mechanisms at play that impact the residual saturation. Based on this study, N_T is an important and convenient, but not complete tool to assess NAPL mobilization. Further investigations into other mechanisms and methods to quantify these mechanisms are needed.

LBM simulations were conducted on simulated sand columns according to different batches of PCE in order to compare with experimental results. The simulated sand columns were set to have the same parameters as the actual columns. In general, the plots of simulation and experimental results were in the same pattern, which reinforced the experimental results and the conclusions made based on the experimental results. Turbulence was found to occur at high flow rates during the simulations. However, based on the experimental and simulation results, a significant impact of turbulence on PCE mobilization was not found, even at the highest flow rate.

BIBLIOGRAPHY

- [1] U.S. Department of the interior, Bureau of Reclamation. (1981). *Ground water manual: A guide for the investigation, development, and management of ground-water resources*. Washington, D.C.: U.S. Dept. of the Interior, Water and Power Resources Service.
- [2] Cheremisinoff, N. P. (2002). *Handbook of water and wastewater treatment technologies*. Boston, MA: Butterworth-Heinemann.
- [3] Bear, J. (1988). *Dynamics of fluids in porous media*. New York, NY: Dover Publications.
- [4] Gleick, P. H. (1993). *Water in crisis: A guide to the world's fresh water resources*. New York, NY: Oxford University Press.
- [5] Kenny, J. F., Barber N. L., Hutson S.S., Linsey K.S., Lovelace, J.K., & Maupin, M.A. (2009). *Estimated use of water in the United States in 2005*. Reston, VA: U.S. Geological Survey.
- [6] Downs, R. M., & Day, F. A. (2005). *National Geographic almanac of geography*. Washington, D.C.: National Geographic.
- [7] Adler, P. M. (1992). *Porous media: Geometry and transports*. Boston, MA: Butterworth-Heinemann.
- [8] Schwarzenbach, R. P., Gschwend, P. M., & Imboden, D. M. (2003). *Environmental organic chemistry*. New York, NY: John Wiley & Sons.
- [9] Gray, W. G., & Miller, C. T. (2014). *Introduction to the thermodynamically constrained averaging theory for porous medium systems*. Heidelberg: Springer.
- [10] Darcy, H. (1856). *Les Fontaines Publiques de la Ville de Dijon*. Paris: Victor Dalmont.
- [11] Todd, D. K., & Mays, L. W. (2005). *Groundwater hydrology*. New York, NY: John Wiley & Sons.
- [12] Li, H. (2006). *Modeling multiphase flow in porous medium systems at multiple scales* (Order No. 3239227). Available from Dissertations & Theses @ University of North Carolina at Chapel Hill; ProQuest Dissertations & Theses Global. (305284343). Retrieved from <http://libproxy.lib.unc.edu/login?url=http://search.proquest.com/docview/305284343?accountid=14244>.
- [13] Mulligan, C., Yong, R., & Gibbs, B. (2001). Surfactant-enhanced remediation of contaminated soil: A review. *Engineering Geology*, 60(1-4), 371-380.

- [14] Rao, P. S., Annable, M. D., Sillan, R. K., Dai, D., Hatfield, K., Graham, W. D., Wood, A. L. & Enfield, C. G. (1997). Field-scale evaluation of *in situ* cosolvent flushing for enhanced aquifer remediation. *Water Resources Research Water Resour. Res.*, 33(12), 2673-2686.
- [15] Josephson, J. (1980). Safeguards for groundwater. *Environmental Science & Technology Environ. Sci. Technol.*, 14(1), 38-44.
- [16] Bedient, P. B., Rifai, H. S., & Newell, C. J. (1999). *Ground water contamination: Transport and remediation*. Upper Saddle River, NJ: PTR Prentice Hall.
- [17] Ward, C. H., Cherry, J. A., & Scalf, M. R. (1997). *Subsurface restoration*. Chelsea, Mich: Ann Arbor Press.
- [18] Boulding, J. R., & Ginn, J. S. (2004). *Practical Handbook of Soil, Vadose Zone, and Ground-Water Contamination: Assessment, Prevention, and Remediation, Second Edition*. Boca Raton, FL: CRC Press.
- [19] Reddy, K. R. (2008). Physical and Chemical Groundwater Remediation Technologies. In C. J. Darnault (Ed.), *Overexploitation and contamination of shared groundwater resources* (pp 257-274). Dordrecht: Springer.
- [20] Yalkowsky, S. H., & He, Y. (2003). *Handbook of Aqueous Solubility Data: An Extensive Compilation of Aqueous Solubility Data for Organic Compounds Extracted from the AQUASOL dATABaSE*. Boca Raton, FL: CRC Press.
- [21] Ladaa, T. I., Lee, C. M., Coates, J. T., & Falta, R. W. (2001). Cosolvent effects of alcohols on the Henry's law constant and aqueous solubility of tetrachloroethylene (PCE). *Chemosphere*, 44(5), 1137-1143.
- [22] Mackay, D., Shiu, W. Y., & Ma, K. C. (1993). *Illustrated handbook of physical-chemical properties and environmental fate for organic chemicals*. Boca Raton, FL: Lewis Publishers.
- [23] McClure, J., Prins, J., & Miller, C. T. (2014). A novel heterogeneous algorithm to simulate multiphase flow in porous media on multicore CPU–GPU systems. *Computer Physics Communications*, 185(7), 1865-1874.
- [24] Dye, A. L., McClure, J. E., Miller, C. T., & Gray, W. G. (2013). Description of non-Darcy flows in porous medium systems. *Physical Review E Phys. Rev. E*, 87(3).
- [25] Dye, A., McClure, J., Gray, W., & Miller, C. T. (2015). Multiscale modeling of porous medium systems. In K. Vafai (Ed.), *Handbook of Porous Media, Third Edition* (pp 3-46). Boca Raton, FL: CRC Press.
- [26] United States Department of Agriculture. (2010). *2007 census of agriculture*. Washington, DC: United States Dept. of Agriculture, National Agricultural Statistics Service.

- [27] National Ground Water Association. (2010). *Groundwater Facts*. Westerville, OH: National Ground Water Association.
- [28] National Research Council. (1993). *In situ bioremediation: When does it work?*. Washington, D.C.: National Academy Press.
- [29] National Research Council. (1997). *Innovations in ground water and soil cleanup: From concept to commercialization*. Washington, D.C.: National Academy Press.
- [30] National Research Council. (1994). *Alternatives for ground water cleanup*. Washington, D.C.: National Academy Press.
- [31] Conrad, S. H., Glass, R. J., & Peplinski, W. J. (2002). Bench-scale visualization of DNAPL remediation processes in analog heterogeneous aquifers: Surfactant floods and *in situ* oxidation using permanganate. *Journal of Contaminant Hydrology*, 58(1-2), 13-49.
- [32] Yuan, Y., & Lee, T. R. (2013). Contact Angle and Wetting Properties. In G. Bracco & B. Holst (Eds.), *Surface Science Techniques* (pp 3-34). Heidelberg: Springer.
- [33] Pennell, K. D., Pope, G. A., & Abriola, L. M. (1996). Influence of Viscous and Buoyancy Forces on the Mobilization of Residual Tetrachloroethylene during Surfactant Flushing. *Environmental Science & Technology Environ. Sci. Technol.*, 30(4), 1328-1335.
- [34] Hauswirth, S. C., Birak, P. S., Rylander, S. C., & Miller, C. T. (2012). Mobilization of Manufactured Gas Plant Tar with Alkaline Flushing Solutions. *Environmental Science & Technology Environ. Sci. Technol.*, 46(1), 426-433.
- [35] Coutelieiris, F. A., & Delgado, J. M. (2012). *Transport processes in porous media*. Heidelberg: Springer.
- [36] Li, Y., Abriola, L. M., Phelan, T. J., Ramsburg, C. A., & Pennell, K. D. (2007). Experimental and Numerical Validation of the Total Trapping Number for Prediction of DNAPL Mobilization. *Environmental Science & Technology Environ. Sci. Technol.*, 41(23), 8135-8141.
- [37] Qian, Y. H., D'huimères, D., & Lallemand, P. (1992). Lattice BGK Models for Navier-Stokes Equation. *Europhysics Letters (EPL) Europhys. Lett.*, 17(6), 479-484.
- [38] Suchomel, E. J., Ramsburg, C. A., & Pennell, K. D. (2007). Evaluation of trichloroethene recovery processes in heterogeneous aquifer cells flushed with biodegradable surfactants. *Journal of Contaminant Hydrology*, 94(3-4), 195-214.
- [39] Reynolds, O. (1895). On the Dynamical Theory of Incompressible Viscous Fluids and the Determination of the Criterion. *Philosophical Transactions of the Royal Society A: Mathematical, Physical and Engineering Sciences*, 186(0), 123-164.

- [40] Davidson, P. A. (2015). *Turbulence: An Introduction for Scientists and Engineers*. Oxford University Press.
- [41] Forchheimer, P. H. (1901). Wasserbewegung durch Boden. *Zeitschrift des Vereines Deutscher Ingenieur*, 45(50), 1782-1788.
- [42] Gray, W. G., & Miller, C. T. (2004). Examination of Darcy's Law for Flow in Porous Media with Variable Porosity. *Environmental Science & Technology Environ. Sci. Technol.*, 38(22), 5895-5901.
- [43] Irmay, S. (1958). On the theoretical derivation of Darcy and Forchheimer formulas. *Trans. AGU Transactions, American Geophysical Union*, 39(4), 702.
- [44] Zeng, Z., & Grigg, R. (2006). A Criterion for Non-Darcy Flow in Porous Media. *Transp Porous Med Transport in Porous Media*, 63(1), 57-69.
- [45] Teng, H., & Zhao, T. (2000). An extension of Darcy's law to non-Stokes flow in porous media. *Chemical Engineering Science*, 55(14), 2727-2735.
- [46] Zhang, C., Werth, C. J., & Webb, A. G. (2008). Investigation of surfactant-enhanced mass removal and flux reduction in 3D correlated permeability fields using magnetic resonance imaging. *Journal of Contaminant Hydrology*, 100(3-4), 116-126.
- [47] Ahemd, N., & Sunada, D. K. (1969). Nonlinear flow in porous media. *Journal of Hydraulics Division, ASCE*, 95(HY6), 1847-1857.
- [48] Chen, Z., Huan, G., & Ma, Y. (2006). *Computational methods for multiphase flows in porous media*. Philadelphia, PA: Society for Industrial and Applied Mathematics.
- [49] Mercer, J. W., & Cohen, R. M. (1990). A review of immiscible fluids in the subsurface: Properties, models, characterization and remediation. *Journal of Contaminant Hydrology*, 6(2), 107-163.
- [50] Brooks, R. H., & Corey, A. T. (1964). *Hydraulic properties of porous media*. Fort Collins, CO: Colorado State University.
- [51] Gray, W. G., & Miller, C. T. (2011). TCAT analysis of capillary pressure in non-equilibrium, two-fluid-phase, porous medium systems. *Advances in Water Resources*, 34(6), 770-778.
- [52] Miller, C. T., Christakos, G., Imhoff, P. T., McBride, J. F., Pedit, J. A., & Trangenstein, J. A. (1998). Multiphase flow and transport modeling in heterogeneous porous media: Challenges and approaches. *Advances in Water Resources*, 21(2), 77-120.
- [53] Thomas, G. W. (1982). *Principles of hydrocarbon reservoir simulation*. Boston, MA: International Human Resources Development.

- [54] Genuchten, M. T. (1980). A Closed-form Equation for Predicting the Hydraulic Conductivity of Unsaturated Soils. *Soil Science Society of America Journal*, 44(5), 892.
- [55] Taylor, T. P., Rathfelder, K. M., Pennell, K. D., & Abriola, L. M. (2004). Effects of ethanol addition on micellar solubilization and plume migration during surfactant enhanced recovery of tetrachloroethylene. *Journal of Contaminant Hydrology*, 69(1-2), 73-99.
- [56] Chevalier, L. R., & Fonte, J. M. (2000). Correlation model to predict residual immiscible organic contaminants in sandy soils. *Journal of Hazardous Materials*, 72(1), 39-52.
- [57] Benzi, R., Succi, S., & Vergassola, M. (1992). The lattice Boltzmann equation: Theory and applications. *Physics Reports*, 222(3), 145-197.
- [58] Chen, S., & Doolen, G. D. (1998). Lattice Boltzmann Method For Fluid Flows. *Annu. Rev. Fluid Mech. Annual Review of Fluid Mechanics*, 30(1), 329-364.
- [59] Aidun, C. K., & Clausen, J. R. (2010). Lattice-Boltzmann Method for Complex Flows. *Annu. Rev. Fluid Mech. Annual Review of Fluid Mechanics*, 42(1), 439-472.
- [60] Saripalli, K. P., Annable, M. D., & Rao, P. S. (1997). Estimation of Nonaqueous Phase Liquid–Water Interfacial Areas in Porous Media following Mobilization by Chemical Flooding. *Environmental Science & Technology Environ. Sci. Technol.*, 31(12), 3384-3388.
- [61] Jackson, A. B. S. (2011). *Multiscale modeling of multiphase flow in porous media using the thermodynamically constrained averaging theory approach* (Order No. 3477468). Available from Dissertations & Theses @ University of North Carolina at Chapel Hill; ProQuest Dissertations & Theses Global. (901112172). Retrieved from <http://libproxy.lib.unc.edu/login?url=http://search.proquest.com/docview/901112172?accountid=14244>.
- [62] Domenico, P. A., & Schwartz, F. W. (1990). *Physical and chemical hydrogeology*. New York, NY: John Wiley & Sons.
- [63] Cohen, R. M., Mercer, J. W., Greenwald, R. M., & Beljin M. S. (1997). *Design guidelines for conventional pump-and-treat systems*. Washington, DC: U.S. Environmental Protection Agency, Office of Research and Development, Office of Solid Waste and Emergency Response.
- [64] Mackay, D. M., & Cherry, J. A. (1989). Groundwater contamination: Pump-and-treat remediation. *Environmental Science & Technology Environ. Sci. Technol.*, 23(6), 630-636.
- [65] U.S. Environmental Protection Agency. (1996). *Pump-and-treat ground-water remediation: A guide for decision makers and practitioners*. Cincinnati, OH: U.S. Environmental Protection Agency, Office of Research and Development, National Risk Management Research Laboratory, Center for Environmental Research Information.

- [66] Cohen, R. M., Vincent, A. H., Mercer, J. W., Faust, C. R., & Spalding, C. P. (1994). *Methods for monitoring pump-and-treat performance*. Ada, OK: Robert S. Kerr Environmental Research Laboratory, Office of Research and Development, U.S. Environmental Protection Agency.
- [67] Roote, D.S. (1997). Technology overview report: *In-situ* flushing. Pittsburgh, PA: Ground-Water Remediation Technologies Analysis Center.
- [68] Villaume, J. F. (1985). Investigations at Sites Contaminated with Dense, Non-Aqueous Phase Liquids (NAPLs). *Ground Water Monitoring & Remediation Ground Water Monitor Remediation*, 5(2), 60-74.
- [69] de Gennes, P. G., François, B.W., & Quéré, D. (2002). *Capillary and Wetting Phenomena: Drops, Bubbles, Pearls, Waves*. (A. Reisinger, Trans.). New York, NY: Springer.
- [70] Adamson, A. W. (1990). *Physical chemistry of surfaces*. New York, NY: John Wiley and Sons.
- [71] Leveen, E. P. (1985). Protecting the Nation's Groundwater from Contamination Office of Technology Assessment. *Environment: Science and Policy for Sustainable Development*, 27(4), 25-27.
- [72] Pope, S. B. (2000). *Turbulent flows*. Cambridge: Cambridge University Press.
- [73] Rott, N. (1990). Note on the history of the Reynolds Number. *Annual Review of Fluid Mechanics*, 22, 1-11.
- [74] Guyon, E. (2001). *Physical hydrodynamics*. Oxford: Oxford University Press.
- [75] Nellis, S. R., Yoon, H., Werth, C. J., Oostrom, M., & Valocchi, A. J. (2009). Surface and Interfacial Properties of Nonaqueous-Phase Liquid Mixtures Released to the Subsurface at the Hanford Site. *Vadose Zone Journal*, 8(2), 343.
- [76] Zheng, J., & Powers, S. E. (2003). Identifying the Effect of Polar Constituents in Coal-Derived NAPLs on Interfacial Tension. *Environmental Science & Technology Environ. Sci. Technol.*, 37(14), 3090-3094.
- [77] Taylor, T. P., Pennell, K. D., Abriola, L. M., & Dane, J. H. (2001). Surfactant enhanced recovery of tetrachloroethylene from a porous medium containing low permeability lenses. *Journal of Contaminant Hydrology*, 48(3-4), 325-350.
- [78] Demond, A. H., & Lindner, A. S. (1993). Estimation of interfacial tension between organic liquids and water. *Environmental Science & Technology Environ. Sci. Technol.*, 27(12), 2318-2331.

- [79] Gillham, R. W., & Rao, P. S. C. (1990). Transport, distribution, and fate of volatile organic compounds in groundwater. In N. M. Ram, R. F. Christman, & K. P. Cantor (Eds.), *Significance and Treatment of Volatile Organic Compounds in Water Supplies* (pp 141-181). Chelsea, MI: Lewis Publishers.
- [80] Lide, D. R. (2016). *CRC Handbook of Chemistry and Physics: A ready-reference book of chemical and physical data, 96th Edition (Internet Version 2016)*. Boca Raton, FL: CRC Press.
- [81] Tzimas, G., Matsuura, T., Avraam, D., Bruggen, W. V., Constantinides, G., & Payatakes, A. (1997). The Combined Effect of the Viscosity Ratio and the Wettability during Forced Imbibition through Nonplanar Porous Media. *Journal of Colloid and Interface Science*, 189(1), 27-36.
- [82] Clifford, J. S., Ioannidis, M. A., & Legge, R. L. (2007). Enhanced aqueous solubilization of tetrachloroethylene by a rhamnolipid biosurfactant. *Journal of Colloid and Interface Science*, 305(2), 361-365.
- [83] Gioia, F., & Urciuolo, M. (2006). Combined effect of Bond and capillary numbers on hydrocarbon mobility in water saturated porous media. *Journal of Hazardous Materials*, 133(1-3), 218-225.
- [84] Larson, R., Davis, H., & Scriven, L. (1981). Displacement of residual nonwetting fluid from porous media. *Chemical Engineering Science*, 36(1), 75-85.
- [85] Taber, J.J. (1981). Research on Enhanced Oil Recovery: Past, Present and Future. In D. O. Shah (Ed.), *Surface Phenomena in Enhanced Oil Recovery* (pp 13-52). New York, NY: Springer.
- [86] Chatzis, I., & Morrow, N. R. (1984). Correlation of Capillary Number Relationships for Sandstone. *Society of Petroleum Engineers Journal*, 24(05), 555-562.
- [87] Morrow, N. R., & Songkran, B. (1981). Effect of Viscous and Buoyancy Forces on Nonwetting Phase Trapping in Porous Media. In D. O. Shah (Ed.), *Surface Phenomena in Enhanced Oil Recovery* (pp 387-411). New York, NY: Springer.
- [88] Morrow, N., Chatzis, I., & Taber, J. (1988). Entrapment and Mobilization of Residual Oil in Bead Packs. *SPE Reservoir Engineering*, 3(03), 927-934.
- [89] Perry, R. H., Chilton, C. H., & Perry, J. H. (1973). *Chemical engineers' handbook*. New York, NY: McGraw-Hill.
- [90] Dawson, H. E., & Roberts, P. V. (1997). Influence of Viscous, Gravitational, and Capillary Forces on DNAPL Saturation. *Ground Water*, 35(2), 261-269.

- [91] Boving, T. B., & Brusseau, M. L. (2000). Solubilization and removal of residual trichloroethylene from porous media: Comparison of several solubilization agents. *Journal of Contaminant Hydrology*, 42(1), 51-67.
- [92] Abriola, L. M., Ramsburg, A., & Pennell, K. D. (2011). Final Report: Development and Optimization of Targeted Nanoscale Iron Delivery Methods for Treatment of NAPL Source Zones. SERDP Project ER-1487
- [93] Abriola, L. M., Goovaerts, P., Pennell, K. D., & Frank E. Löffler. (2008). Technical Report: Development of Assessment Tools For Evaluation of the Benefits of DNAPL Source Zone Treatment. SERDP Project ER-1293
- [94] Duffield, A. R., Ramamurthy, R. S., & Campanelli, J. R. (2003). Surfactant enhanced mobilization of mineral oil within porous media. *Water, Air, and Soil Pollution*, 143, 111–122.
- [95] Aydin, G. A., Agaoglu, B., Kocasoy, G., & Coptý, N. K. (2011). Effect of temperature on cosolvent flooding for the enhanced solubilization and mobilization of NAPLs in porous media. *Journal of Hazardous Materials*, 186(1), 636-644.
- [96] Padgett, P. K., & Hayden, N. J. (1999). Mobilization of residual tetrachloroethylene during alcohol flushing of clay-containing porous media. *Journal of Contaminant Hydrology*, 40(3), 285-296.